



AD-A141468

NAVENVPREDRSCHFAC  
TECHNICAL REPORT  
TR 84-01

LIBRARY  
RESEARCH REPORTS DIVISION  
NAVAL POSTGRADUATE SCHOOL  
MONTEREY, CALIFORNIA 93943

# A SPIRAL ANALYSIS TECHNIQUE FOR MONITORING AND PREDICTING TROPICAL CYCLONE INTENSITY USING SATELLITE DATA

**Bernard John Cook**

Naval Environmental Prediction Research Facility

**FEBRUARY 1984**

APPROVED FOR PUBLIC RELEASE  
DISTRIBUTION UNLIMITED



**NAVAL ENVIRONMENTAL PREDICTION RESEARCH FACILITY**  
**MONTEREY, CALIFORNIA 93943**

NAVENVPREDRSCHFAC TR 84-01

AN (1) AD-A141 468  
 PS (2) 040200  
 CI (3) (U)  
 CA (5) NAVAL ENVIRONMENTAL PREDICTION RESEARCH FACILITY  
 MONTEREY CA  
 TI (6) A Spiral Analysis Technique for Monitoring and  
 Predicting Tropical Cyclone Intensity Using Satellite  
 Data.  
 TC (8) (U)  
 DN (9) Final rept.,  
 AU (10) Cook, B. J.  
 RD (11) Feb 1984  
 PG (12) 107p  
 RS (14) NEPRF-IR-84-01  
 PJ (16) F59551  
 RC (20) Unclassified report  
 DE (23) \*Tropical cyclones, intensity, weather forecasting,  
 Aerial photographs, Meteorological satellites, Image  
 processing, Clouds, Patterns, Curves(Geometry),  
 Statistical analysis  
 DC (24) (U)  
 ID (25) Satellite photography, Spiral, WU6217, FE62759N  
 IC (26) (U)  
 AB (27) A spiral analysis technique is developed which  
 quantifies the spiral patterns of cloud bands observed  
 in IR satellite images of tropical cyclones. The  
 technique utilizes the Navy's SPADS (Satellite Data  
 Processing and Display System) minicomputer for  
 processing the digital IR data. The technique consists  
 of best fitting spherical-logarithmic spirals to  
 tropical cyclone spiral cloud bands and performing  
 multiple Fourier analyses of the radiance field along  
 spirals orthogonal to the bands. Linear regression  
 techniques are used to establish a relationship between  
 spiral parameters derived from the Fourier analyses and  
 tropical cyclone intensity. Algorithms for current  
 intensity, and 12 and 24 h forecasts are developed.  
 Tests on an independent data set show significant skill  
 in estimating current intensity and in making 12 h  
 forecasts. The most important predictors selected are  
 persistence and parameters related to the dominant  
 spiral signal and maximum IR count of the analyzed  
 radiance field. Biases in the forecast algorithms  
 suggest that other parameters are necessary to more  
 accurately predict tropical cyclone intensity. The  
 results, however, demonstrate the usefulness of the  
 technique as an aid to tropical cyclone forecasters.  
 AC (28) (U)  
 DL (33) 01  
 SE (34) F  
 CC (35) 487279



UNCLASSIFIED

SECURITY CLASSIFICATION OF THIS PAGE (When Data Entered)

REPORT DOCUMENTATION PAGE		READ INSTRUCTIONS BEFORE COMPLETING FORM
1. REPORT NUMBER NAVENVPREDRSCHFAC Technical Report TR 84-01	2. GOVT ACCESSION NO.	3. RECIPIENT'S CATALOG NUMBER
4. TITLE (and Subtitle) A Spiral Analysis Technique for Monitoring and Predicting Tropical Cyclone Intensity Using Satellite Data		5. TYPE OF REPORT & PERIOD COVERED Final
7. AUTHOR(s) Bernard John Cook		6. PERFORMING ORG. REPORT NUMBER TR 84-01
9. PERFORMING ORGANIZATION NAME AND ADDRESS Naval Environmental Prediction Research Facility Monterey, CA 93943		8. CONTRACT OR GRANT NUMBER(s)
11. CONTROLLING OFFICE NAME AND ADDRESS Naval Air Systems Command Department of the Navy Washington, DC 20361		10. PROGRAM ELEMENT, PROJECT, TASK AREA & WORK UNIT NUMBERS PE 62759N PN WF59-551 TA 2 NEPRF WU 6.2-17
14. MONITORING AGENCY NAME & ADDRESS (if different from Controlling Office)		12. REPORT DATE February 1984
		13. NUMBER OF PAGES 104
		15. SECURITY CLASS. (of this report) UNCLASSIFIED
		15a. DECLASSIFICATION/DOWNGRADING SCHEDULE
16. DISTRIBUTION STATEMENT (of this Report)  Approved for public release; distribution unlimited.		
17. DISTRIBUTION STATEMENT (of the abstract entered in Block 20, if different from Report)		
18. SUPPLEMENTARY NOTES		
19. KEY WORDS (Continue on reverse side if necessary and identify by block number) Tropical cyclone Intensity forecasting Spiral analysis Satellite analysis		
20. ABSTRACT (Continue on reverse side if necessary and identify by block number) A spiral analysis technique is developed which quantifies the spiral patterns of cloud bands observed in IR satellite images of tropical cyclones. The technique utilizes the Navy's SPADS (Satellite Data Processing and Display System) minicomputer for processing the digital IR data. The technique consists of best fitting spherical-logarithmic spirals to tropical cyclone spiral cloud bands and performing multiple Fourier analyses of the radiance field along spirals orthogonal to the bands. ((Continued on reverse))		

DD FORM 1 JAN 73 1473

EDITION OF 1 NOV 65 IS OBSOLETE  
S/N 0102-014-6601

UNCLASSIFIED

SECURITY CLASSIFICATION OF THIS PAGE (When Data Entered)

Block 20, Abstract, continued.

Linear regression techniques are used to establish a relationship between spiral parameters derived from the Fourier analyses and tropical cyclone intensity. Algorithms for current intensity, and 12 and 24 h forecasts are developed.

Tests on an independent data set show significant skill in estimating current intensity and in making 12 h forecasts. The most important predictors selected are persistence and parameters related to the dominant spiral signal and maximum IR count of the analyzed radiance field.

Biases in the forecast algorithms suggest that other parameters are necessary to more accurately predict tropical cyclone intensity. The results, however, demonstrate the usefulness of the technique as an aid to tropical cyclone forecasters.

## CONTENTS

Chapter 1. Introduction	
1.1 Statement of the Problem	1
1.2 Objective	2
1.3 Approach	2
Chapter 2. A Survey of Past Studies of the Relationship of Cloud Patterns to Tropical Cyclone Intensity	
2.1 Observed Spiral Patterns	3
2.2 Satellite-Derived Estimates and Predictions of Tropical Cyclone Intensity	5
Chapter 3. Development of Methodology	
3.1 Spiral Analysis Technique	12
3.1.1 Determination of the Spiral Analysis Grid	13
3.1.2 Spiral-Fourier Analysis of the IR Radiance Field	23
3.2 Statistical Analysis	27
3.2.1 Selection of Potential Predictors	27
3.2.2 Calculation of Regression Equations	32
3.2.3 Independent Tests	32



Chapter 4. Data	
4.1 Dependent Data Set	35
4.1.1 Satellite Imagery	35
4.1.2 Ground Truth Data	38
4.2 Independent Data Set	39
4.2.1 Satellite Imagery	39
4.2.2 Ground Truth Data	40
Chapter 5. Results	
5.1 Current Intensity (VMAX)	50
5.2 12 h Forecast Intensity (VP12)	56
5.3 24 h Forecast Intensity (VP24)	61
Chapter 6. Conclusions and Recommendations	
6.1 Conclusions	68
6.2 Recommendations for Future Work	69
Appendix A TEDS Software Documentation	72
Appendix B Governing Equations	83
Appendix C Descriptions of the Cyclones of the	
Dependent Data Set	90
References	96
Acknowledgements	99
Distribution	100

## 1. INTRODUCTION

### 1.1 STATEMENT OF THE PROBLEM

The ability to monitor and predict the intensity<sup>1</sup> of tropical cyclones is important because of the death and destruction caused by the high wind speeds, storm surges, and heavy precipitation which characterize these cyclones (Anthes, 1982). Tropical cyclones occur over the warm tropical oceans where they usually affect coastal habitations and ships at sea. Because of the sparse synoptic reporting network in these areas, an important source of tropical cyclone intensity data is reconnaissance by aircraft. However, in recent years as aircraft reconnaissance has been reduced for economic reasons, an effort has been made to fill the resulting data gaps by using meteorological satellite information (Gentry et al., 1980).

Among all meteorological satellites, the geostationary satellites are particularly suited for tropical cyclone data collection. Because they image the same disk of the Earth every half-hour they acquire data more often than is feasible using aircraft reconnaissance. The usable data collected are the infrared (IR) radiance count values which can be converted to equivalent blackbody cloud top temperatures (Gentry et al., 1980).

---

<sup>1</sup>Defined as the maximum sustained surface wind speed.

In the past, the satellite information has been interpreted in terms of the spiral-shaped cloud patterns of tropical cyclones (Arnold, 1977). Dvorak (1975) empirically related the patterns to tropical cyclone intensity by using visible and IR satellite images. However, with the development of interactive computer techniques for manipulating satellite data, it has become evident that the relationship of the cloud patterns in the digital IR data to tropical cyclone intensity can be better quantified.

## 1.2 OBJECTIVE

The specific purpose of this study is to determine a quantitative relationship between satellite measurements of the IR radiance field and the operationally reported intensity of tropical cyclones.

## 1.3 APPROACH

The approach to the problem consists of three steps:

i) A detailed survey of past studies to gain an insight into the relationship of observed spiral-shaped cloud patterns to tropical cyclone intensity.

ii) The development of the methodology to apply the past research findings to extract the relevant parameters from the digital IR radiance field.

iii) The development and testing of multiple linear regression equations for monitoring and predicting tropical cyclone intensity using the extracted parameters.



## 2. A SURVEY OF PAST STUDIES OF THE RELATIONSHIP OF CLOUD PATTERNS TO TROPICAL CYCLONE INTENSITY

### 2.1 OBSERVED SPIRAL PATTERNS

In studies of radar films of tropical cloud features Senn and Hiser (1959) found that hurricanes are characterized by asymmetric rain bands that generally conform to logarithmic spirals. The equation of a logarithmic spiral is

$$\ln r = -\alpha \theta \quad (1)$$

where  $r$  is the radius,  $\alpha$  is the inflow or crossing angle that the spiral makes with concentric circles about the spiral center, and  $\theta$  is the azimuth. They found that these spiral rain bands usually extended 100 to 200 km from the cyclone center, and that there were often several spiral bands associated with each cyclone. The spiral cloud bands were composed of numerous large cellular convective clouds that propagated along the band towards the spiral center.

Lahiri (1981) used a simple model of a tropical cyclone in which the low-level streamlines were logarithmic spirals and showed that the rate of generation of latent heat in the model was proportional to  $\alpha$ . Lahiri observed that many satellite images of tropical cyclones exhibit cloud banding patterns that conform to logarithmic spirals and assumed that the cloud band spirals were coincident with the

streamline spirals. Lahiri then showed that the spiral cloud bands degenerated to circles ( $\alpha$  approached zero) as the cyclones matured.

The relationship between latent heating and cloud patterns is important because the latent heat released within deep cumulus towers is the tropical cyclone's primary energy source (Anthes, 1982). The satellite senses the IR radiance field of the tropical cyclone and its environment. The radiance values for the cloud tops can be converted to equivalent blackbody cloud top temperatures which can provide quantitative information on the availability of latent heat within the cyclone (Gentry et al., 1980). Therefore, the latent heat released in a cyclone is indicated by the amount and strength of the convection, which are related to the areal distribution of the cyclone's satellite-derived IR radiance field.

In a linear stability analysis of the development of spiral cloud bands in tropical cyclones Kurihara (1976) found that the preferred spiral scale of the large scale bands was wavenumber two with a band width of 200 km. The flow perturbation fields of spiral shape were modeled by logarithmic spirals with modifying Bessel functions. Willoughby (1978) showed a linear model of hurricane rain bands in cylindrical, log-pressure coordinates that generated a physically realistic radial geopotential structure with waves of wavenumber two and higher.

Black and Anthes (1971) quantified the spiral structure of the tropical cyclone outflow layer by harmonic analysis of the tangential and radial components of the satellite derived flow fields. Their analysis of five tropical cyclones showed the most significant number of spiral bands to be less than four and that the horizontal scale of the bands increased outward from the storm center. In a more recent study, Rodgers and Gentry (1983) traced the upper and lower tropospheric wind fields around three tropical cyclones from satellite-derived cloud drift winds. They found that the flow at both levels revealed a large scale spiral structure. They used the fields to compute the local changes in the cyclone's net relative angular momentum and found that it appeared to be related to the trend in storm intensity.

## 2.2 SATELLITE-DERIVED ESTIMATES AND PREDICTIONS OF TROPICAL CYCLONE INTENSITY

Techniques for estimating and predicting the intensity of tropical cyclones from satellite IR or visible pictures focus on the identification of various tropical cloud features, such as the shape and areal extent of the cirrus overcast, the appearance of the eye, and the amount of cloud banding present (Fett, 1966; Fritz et al., 1966; Hubert et al., 1969; Dvorak, 1973, 1975, and 1979). The widely used Dvorak (1975) method is recognized as the most accurate subjective technique for estimating the current and future



intensity of tropical cyclones using satellite imagery (Shewchuk and Weir, 1980). The basic premise of Dvorak's technique is that by associating the organization of the various cloud features of tropical cyclones with their intensities, estimates of the current and future intensities for similarly organized cyclones can be obtained.

Figure 1 shows the characteristic, satellite-observed cloud features that are related to tropical cyclone intensity by Dvorak's method. The central cloud features (CF) refer to the extent and shape of the cloud elements that appear within the curve of the comma band and can either surround or cover the storm center. Intensification is indicated by the CF becoming colder, or by the eye becoming either warmer, smaller, or more circular. The cyclone's outer banding features (BF) in Figure 1 refer to the outer comma shaped cloud band that curves evenly around the central features. Intensification is indicated by the BF becoming more developed.

In the application of the technique the CF and BF are evaluated and their results combined to provide a "T-number" description of the intensity of a cyclone. The assigned T-number is plotted on a development diagram (see Fig. 2) and the cyclone is expected to intensify or weaken according to one of the three curves plotted. Rapidly developing or rapidly weakening cyclones ( $\pm 1.5$  T-numbers per day) are plotted on the RAPID curve, cyclones exhibiting normal

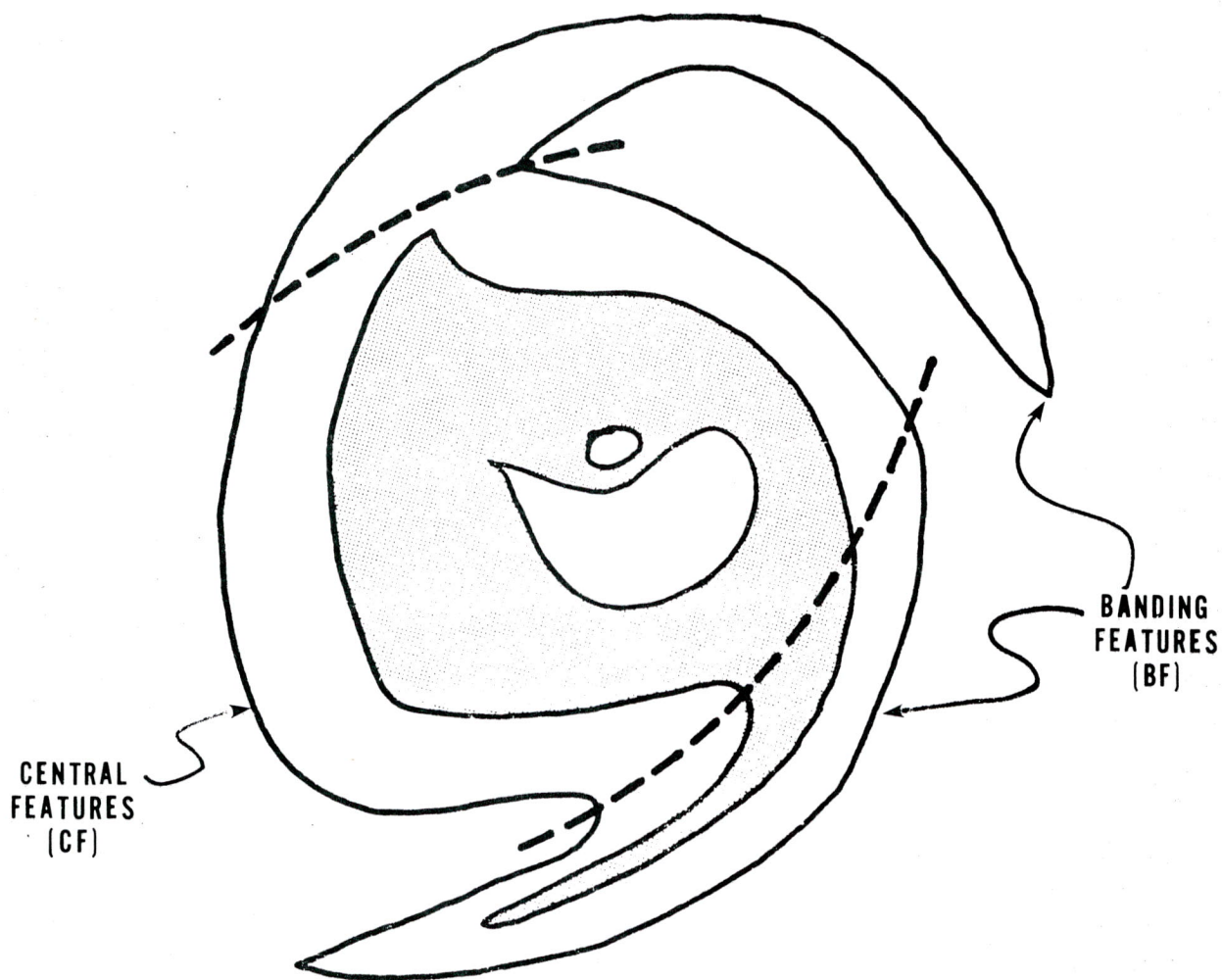


Figure 1. A schematic of a typical IR satellite image showing the different cloud features which are related to tropical cyclone intensity by Dvorak's (1979) method. The contours are isolines of equal gray shades. The contour values increase towards the cyclone center and are inversely proportional to the temperatures of the cloud tops. The circular area in the center of the cyclone is the warm eye. The area inside of the dashed lines, the cloud features encircling the eye, are the central features (CF). The cloud bands outside of the dashed lines are the banding features (BF).

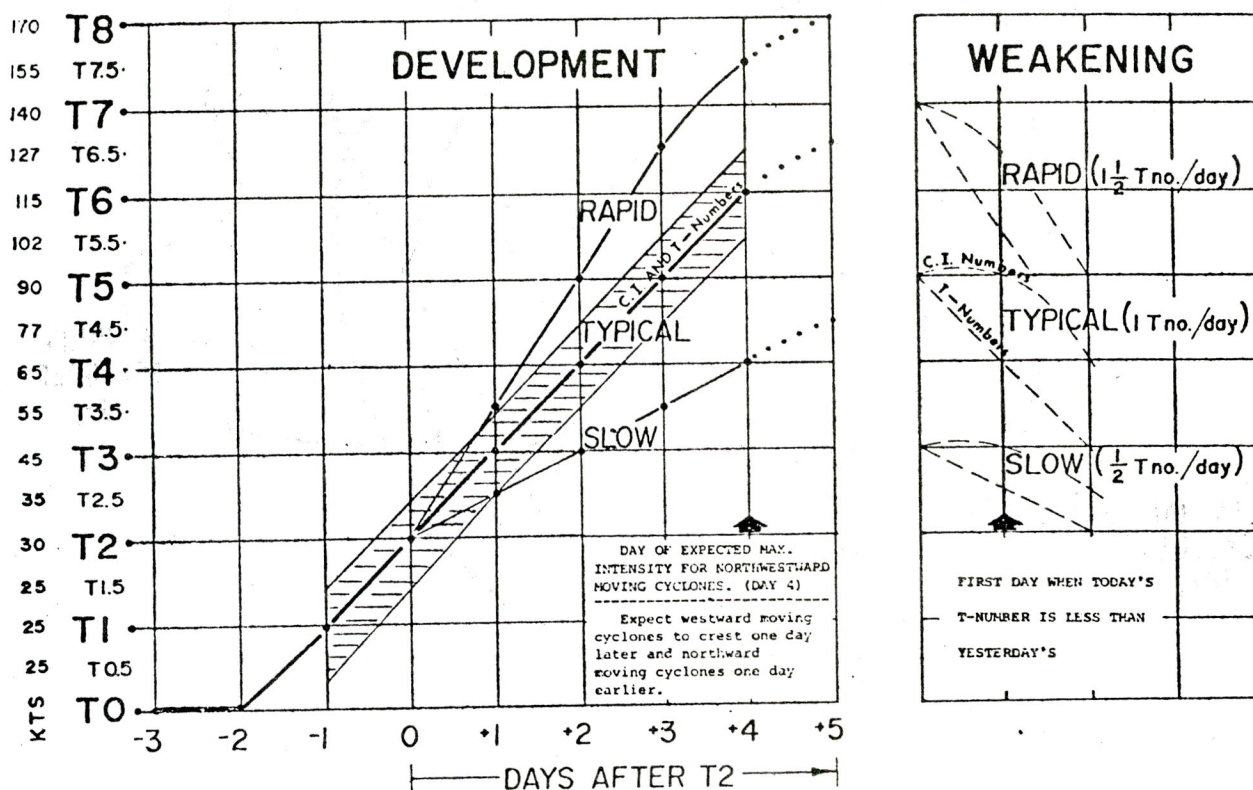


Figure 2. Intensity change curves of the Dvorak (1975) model. The T (for tropical) numbers are defined in terms of the cloud features of the storm and relate to the storm's intensity. The curves depict tropical cyclone development and weakening as occurring along one of the three curves of T-number vs. time. A typical 24 h change is one T-number (Dvorak, 1975). The relationship between the T-numbers and the maximum sustained surface wind speed is shown to the left in the figure.



developing or weakening ( $\pm 1.0$  T-numbers per day) are plotted on the TYPICAL curve, and slowly developing or slowly weakening cyclones ( $\pm 0.5$  T-numbers per day) are plotted on the SLOW curve. A 24 h forecast is made by incrementing the abscissa one day along the cyclone's characteristic curve. The C.I. number (current intensity) on the WEAKENING portion of the figure is a modified T-number to account for factors which are not directly related to the BF or CF (see Dvorak, 1975). The relationship between T-number and maximum surface wind speed can be seen in the left of the figure. Note that the larger T-numbers encompass a wide range of wind speeds.

An objective method of predicting tropical cyclone intensity by using computer processed IR satellite data has been developed by Gentry et al. (1980). Radially averaged equivalent blackbody cloud top temperatures (derived from the IR radiance field) about the cyclone center and their standard deviations were used to make 24 h predictions of tropical cyclone intensity via linear regression equations. They found that the relationship of the IR data to future intensity was nonlinear over time. Consequently, their best results were reported when the data were stratified based on the current intensity, which was estimated by using the Dvorak (1975) technique. The tropical cyclones were stratified into two groups: current intensity less than or

equal to 65 kt and current intensity greater than 65 kt. Gentry et al. (1980) concluded that the areal distribution of the IR radiance field serves as an index of the organization of the cyclone's convective activity and that the relationship can be successfully exploited to predict tropical cyclone intensity.

Swadley (1983) used a spiral linearization technique (SLT) on an interactive computer to transform IR satellite images of the cloud bands of tropical cyclones into logarithmic spiral coordinates. Using a limited number of satellite images, Swadley developed linear regression equations for estimating tropical cyclone intensity based on the spiral inflow angle ( $\alpha$ ) and three measurements of the IR radiance field. He found that the equations could not explain the observed variability of intensity between the cyclones and concluded that more information from the digital IR satellite data was necessary in order to develop a better relationship with tropical cyclone intensity.

Using a large number of satellite images processed by the SLT, Peterson et al. (1983) evaluated the statistical relationship between  $\alpha$  and tropical cyclone intensity. They showed that  $\alpha$  behaved randomly with time, contrary to Lahiri's (1981) findings, and concluded that it was impossible to characterize the intensity of a tropical cyclone using a single parameter.

In summary, past research has shown that tropical cyclone cloud bands are characterized by a low wavenumber spiral pattern. The spiral-shaped cloud bands are observed in IR satellite data and have been empirically related to tropical cyclone intensity.

Recently, satellite data manipulation techniques on interactive computers have shown promise for better quantifying the relationship of the cloud bands to tropical cyclone intensity. The method that shows the most promise is spiral analysis coupled with multiple linear regression.



### 3. DEVELOPMENT OF METHODOLOGY

In the present chapter linear regression techniques are used to establish a relationship between the spiral-shaped cloud bands and the intensity of tropical cyclones. A major step in the process is the development of a spiral analysis technique to quantify the spiral patterns of the cloud bands. In this method the spiral characteristics are extracted from the satellite-derived digital IR data using multiple Fourier analyses. The Fourier analyses are performed over a spiral grid which is unique to each image of a tropical cyclone.

This particular technique was chosen because it incorporates the large scale spiral shape of the cloud bands into the Fourier analyses. The technique differs from previous techniques (e.g., Swadley, 1983) in that it is performed in geographic coordinates instead of local polar coordinates, and the data are analyzed in place instead of being transformed into spiral coordinates. Therefore, there is no distortion due to the curvature of the earth or coordinate transforms.

#### 3.1 SPIRAL ANALYSIS TECHNIQUE

Each digital IR satellite image processed in the present study was analyzed on the Satellite-data Processing and Display System (SPADS) Eclipse S-250 minicomputer at the Naval Environmental Prediction Research Facility (NEPRF).

The unique capabilities of the SPADS for interactive digital image processing are described by Schramm et al. (1982).

The relevant subroutines of the computer program (TEDS) written for this study to implement the spiral analysis technique on the SPADS are reproduced in Appendix A. TEDS utilizes an algorithm adapted from Nicholson (1983) to determine the spiral analysis grid for an image and to perform the Fourier analyses of the IR satellite data over the spiral grid.

#### 3.1.1 Determination of the Spiral Analysis Grid

Figure 3 is an example of a typical spiral analysis grid. The grid is defined as ten parallel spirals of data points which have a common center and inflow angle ( $\alpha$ ). The spirals are separated from each other by  $18^\circ$  and are orthogonal to the cloud bands. The inflow angle and spiral center of the spiral analysis grid are determined by an average of the spiral fits to all of the cloud bands processed on a particular image. The processing consists of calculating the best least squares fit spiral corresponding to each cloud band and then averaging them. The detailed procedure is as follows: after displaying the image on the video monitor, the image coordinates (lines, elements) of the cloud band are entered into TEDS via the interconnected graph pen/tablet. The pen is drawn along the center

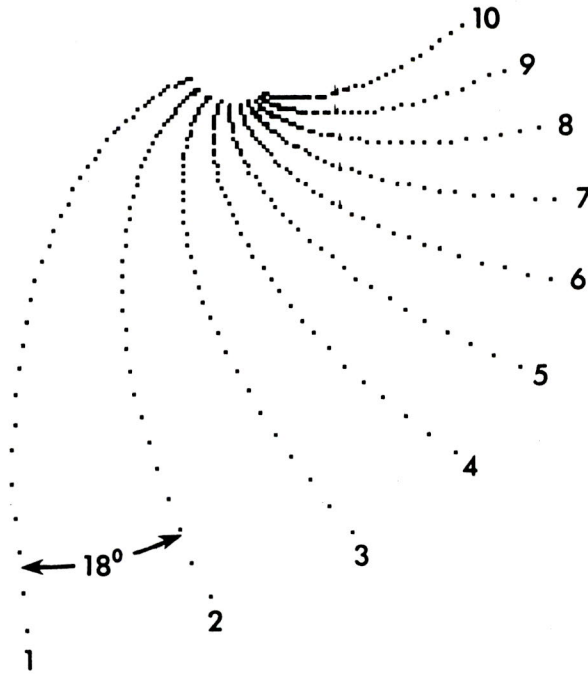


Figure 3. The dots represent a typical spiral analysis grid used in this study. Each dot represents a data point. The grid consists of ten parallel spiral rows of data points which have a common center (not shown) and are orthogonal to the cloud bands. Each spiral has the same inflow angle  $\alpha$  and is separated from its neighbors by  $18^\circ$ . How the grid is determined and oriented on an image is described later in the text.



of the cloud band, parallel to the edge, starting at its outermost point and working inwards toward the center (see Fig. 4).

The entered coordinates are earth-located (navigated) and a spherical-logarithmic spiral is least squares fitted to them following Nicholson (1982). This process is thoroughly described in Appendix B. Figure 5 is a mercator plot of a spherical-log spiral and its representation in spiral coordinates. The equation of a spherical-log spiral is

$$\mu = 2 \arctan\left(\tan\left(\frac{\mu_0}{2}\right) e^{-\tan\alpha(v-v_0)}\right), \quad (2)$$

where  $\mu$  is the great circle distance, and  $v$  the angular separation, between points along the spiral and the spiral center;  $\mu_0$  and  $v_0$  refer to the same quantities at the outermost point along the spiral and  $\alpha$  is the inflow angle of the spiral.

Since there are three unknowns ( $\alpha$ ,  $\mu_0$ , and  $v_0$ ) and the least squares formulation yields only two normal equations, an iterative computational scheme is used to calculate one variable. The normal equations are most easily solved for  $\alpha$  and  $v_0$ , therefore,  $\mu_0$  is determined using a highly efficient iterative computational scheme following Nicholson (1982). The iterative scheme is used to converge on the best fit spiral center, which uniquely determines  $\mu_0$ .

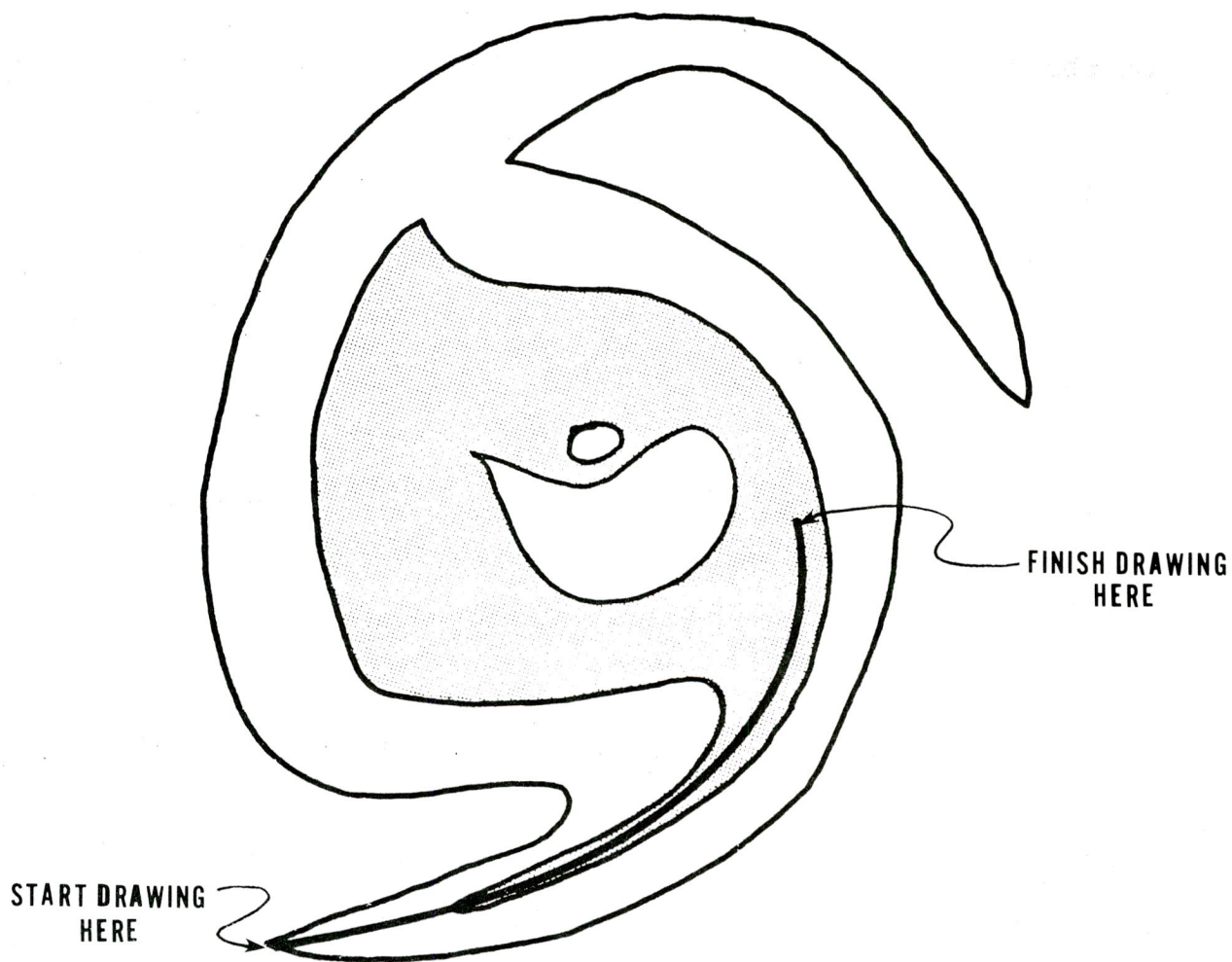


Figure 4. The heavy line shown with starting and ending points is the tracing of the graph pen along the center of the schematically represented cloud band. In this example, the cloud band can be traced no farther towards the cyclone center (eye).

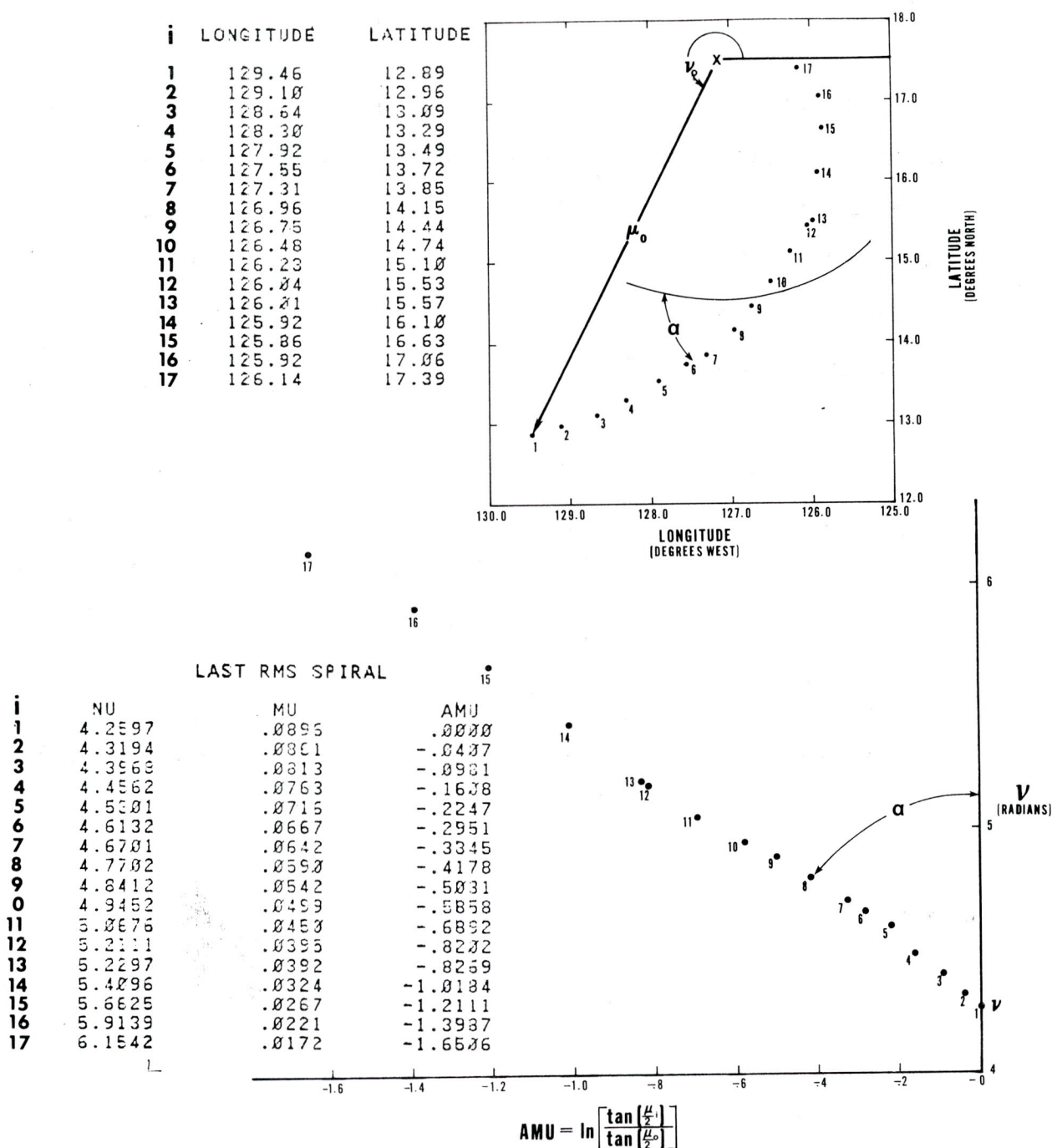


Figure 5. The inset is a mercator plot of the data points entered along the heavy line shown in Fig. 4. An X marks the best fit spiral center and, thus, defines  $\mu_0$  and  $\nu_0$ . The equation of a spherical-log spiral is  $\mu = 2 \arctan [\tan(\mu_0/2) \exp(-\tan \alpha (\nu - \nu_0))]$ . An arc of a circle about the spiral center is shown, defining  $\alpha$ , which is  $41^\circ$ . The bottom graph are the data points shown in the inset plotted in spherical-log spiral coordinates. The representation of  $\alpha$  in the spiral coordinates is also shown.



The upper left and lower right corners of the area in which to search for the spiral center are entered from the graph tablet (see Fig. 6). The search area is divided into a six-by-six grid and each interior grid point used as a sample spiral center. The following solutions to the normal equations (Appendix B) are then solved for  $v_o$  and  $\alpha$ :

$$\cot \alpha = \frac{\sum_{i=1}^N v_i \sum_{i=1}^N \ln T_i - N \sum_{i=1}^N v_i \ln T_i}{N \sum_{i=1}^N (\ln T_i)^2 - \left( \sum_{i=1}^N \ln T_i \right)^2}, \quad (3)$$

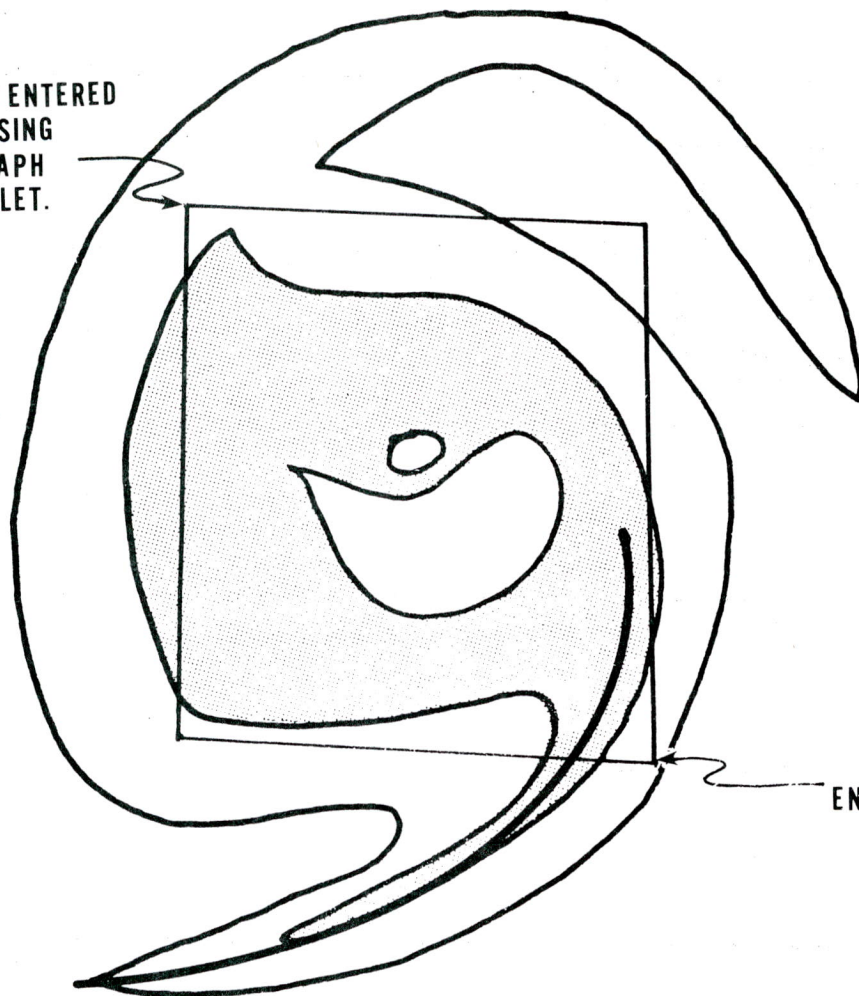
$$v_o = \frac{\sum_{i=1}^N v_i \sum_{i=1}^N (\ln T_i)^2 - \sum_{i=1}^N \ln T_i \sum_{i=1}^N v_i \ln T_i}{N \sum_{i=1}^N (\ln T_i)^2 - \left( \sum_{i=1}^N \ln T_i \right)^2} \quad (4)$$

where

$$T_i = \frac{\tan\left(\frac{\mu_i}{2}\right)}{\tan\left(\frac{\mu_o}{2}\right)}.$$

The iterative scheme continues as the sample spiral center with the smallest root mean square error is focused on as the new grid center and the grid size divided by six. Figure 7 is a schematic of the process, showing three of the nine iterations used to bring the grid spacing to image resolution. This minimizes the RMS error while determining

THIS POINT ENTERED  
FIRST USING  
THE GRAPH  
PEN/ TABLET.



THIS POINT  
ENTERED SECOND  
USING THE  
GRAPH PEN/  
TABLET.

Figure 6. The upper left and lower right coordinates of the area in which to search for the spiral center of the entered heavy line are entered via the graph pen/tablet. The drawn box is a spherical quadrilateral whose coordinates are calculated and displayed by TEDS. The size of the box is arbitrary.

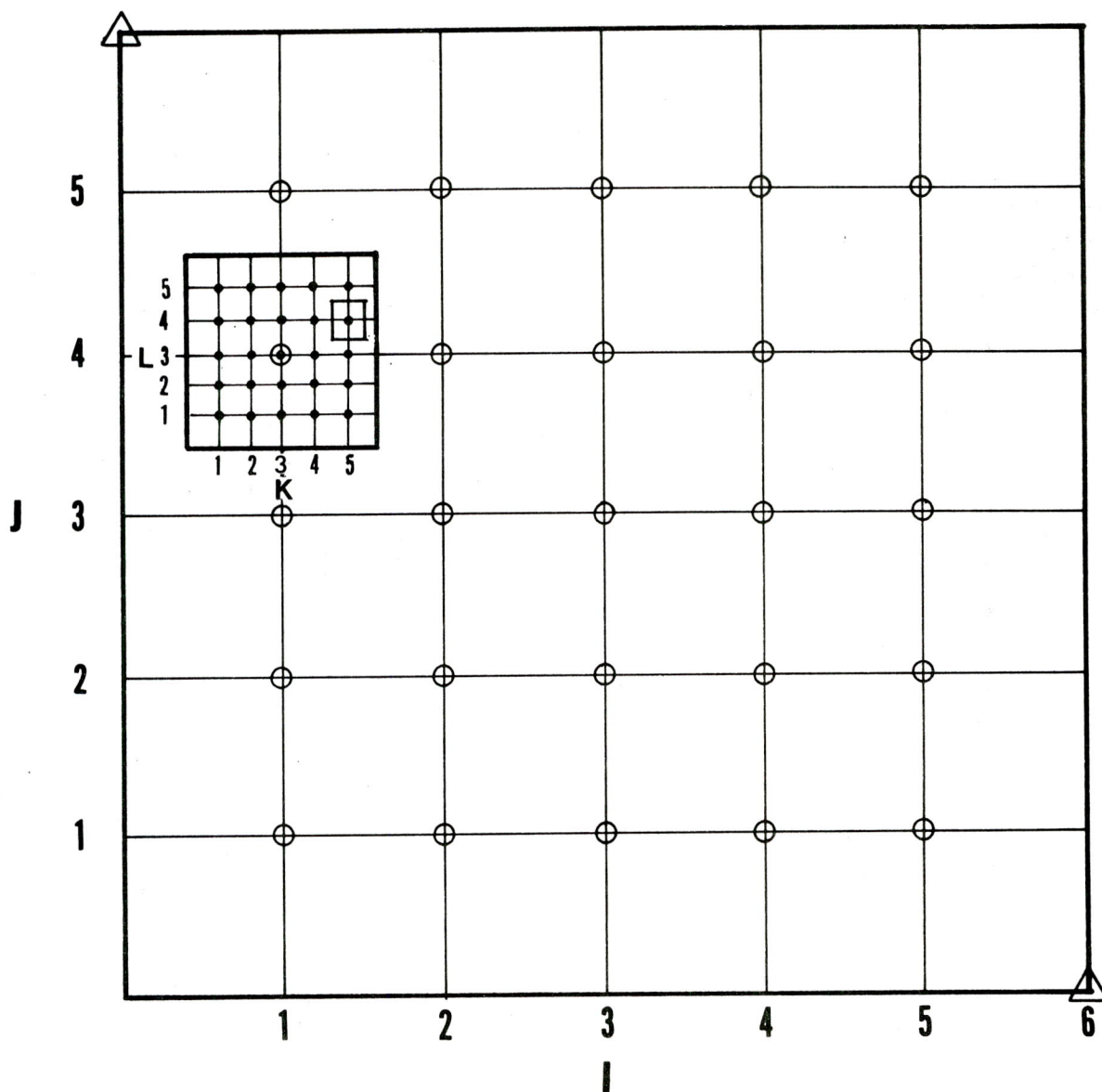


Figure 7. A mercator representation of the box described in Fig. 6. The triangles at the corners represent the user entered points. The box is divided into a 6×6 grid and the 25 interior points (circled) are used as sample spiral centers and their RMS error calculated. Assuming the point I1,J4 has the smallest RMS error, it is focused on as the new grid center and the grid size is divided further by six. The process is repeated on the new grid (solid dots), and assuming the point K5,L4 has the smallest RMS error, it is focused on as the new grid center and the grid size divided by six again. The process is repeated nine times to bring the grid spacing to image resolution.



$\alpha$ ,  $\mu_0$ ,  $\nu_0$ , and the latitude and longitude of the best fit spiral center.

The five parameters calculated from the input line along the cloud band are then used to reconstruct the best fit spherical-log spiral on the video monitor. Using the plotted spiral fit and RMS error statistic as data quality checks, the operator then decides whether or not to save the calculated data for use in the determination of the spiral analysis grid. During processing, the inflow angles and spiral centers saved by the operator are averaged. As noted earlier, the averaged quantities determine the spiral characteristics of the analysis grid.

The final step in the process of determining the spiral analysis grid is orienting it properly on the image so that the desired cloud pattern is Fourier analyzed. The orientation is accomplished by defining a delimiting spiral with the graph pen. As shown in Figure 8, the delimiting spiral has the averaged center and inflow angle described above, however, it is rotated with respect to the cloud pattern to be analyzed:  $\mu_0$  and  $\nu_0$  are selected such that the cloud pattern of interest is located between the spiral center and the delimiting spiral.

An important point is that in spiral coordinates the delimiting spiral is orthogonal to the ten spirals which comprise the analysis grid. The delimiting spiral only defines the orientation of the grid on the image.

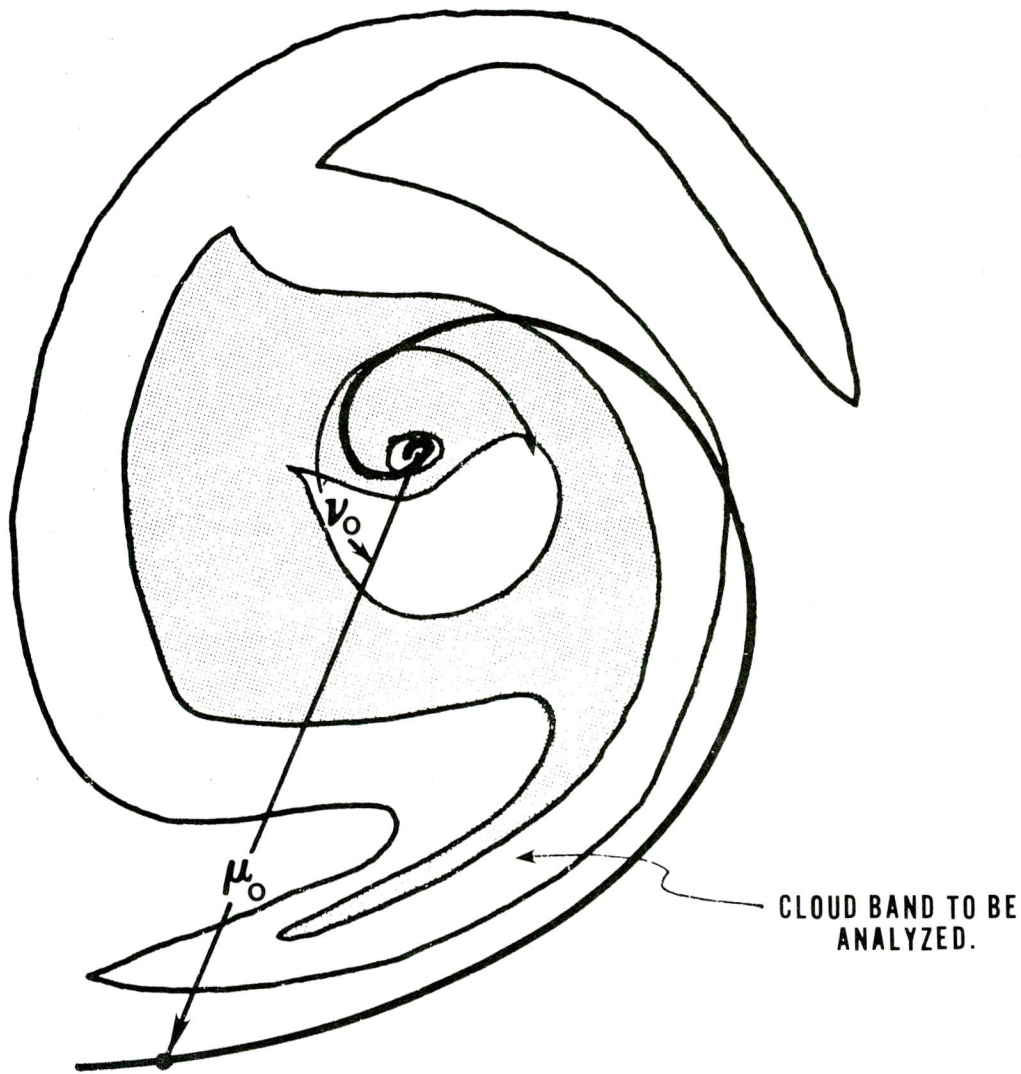


Figure 8. The heavy line is the delimiting spiral of the tropical cyclone and defines the orientation of the spiral analysis grid. The latitude and longitude of its center, and its inflow angle  $\alpha$ , are those of the average of all of the cloud bands processed.  $\mu_0$  and  $\nu_0$  are selected such that the cloud band to be analyzed is located between the spiral center and the delimiting spiral.  $\nu_0$  is measured counterclockwise from a latitude circle.

### 3.1.2 Spiral-Fourier Analysis of the IR Radiance Field

In order to quantify the spiral patterns of the cloud bands multiple spiral-Fourier analyses (Fourier analyses along spherical-log spirals) are used. The analyses are performed over the spiral grid, along the ten spirals orthogonal to the delimiting spiral (see Fig. 9). Therefore, the Fourier analyses decompose the IR radiance field into spiral harmonics parallel to the delimiting spiral (see Fig. 10).

The spiral-Fourier analyses proceed as follows: along each of the orthogonal spirals of the grid the geographic locations of forty equally spaced data points are calculated. In spiral coordinates distances are measured as a function of the natural logarithm of the radius, therefore, data points separated by equal intervals physically become farther apart as they are sampled farther from the spiral center. As the data are sampled closer to the spiral center (as the radius goes to zero) they become indistinguishable on the finite resolution image. In order to avoid this difficulty, data are not sampled along an orthogonal spiral until the orthogonal spiral has passed beyond the inner portion of the delimiting spiral (see Figs. 9 and 10).

After the locations of the forty data points along the orthogonal spiral are calculated, their IR radiance values are retrieved and their conventional equal spaced discrete Fourier transform is calculated (Panofsky and Brier, 1968).

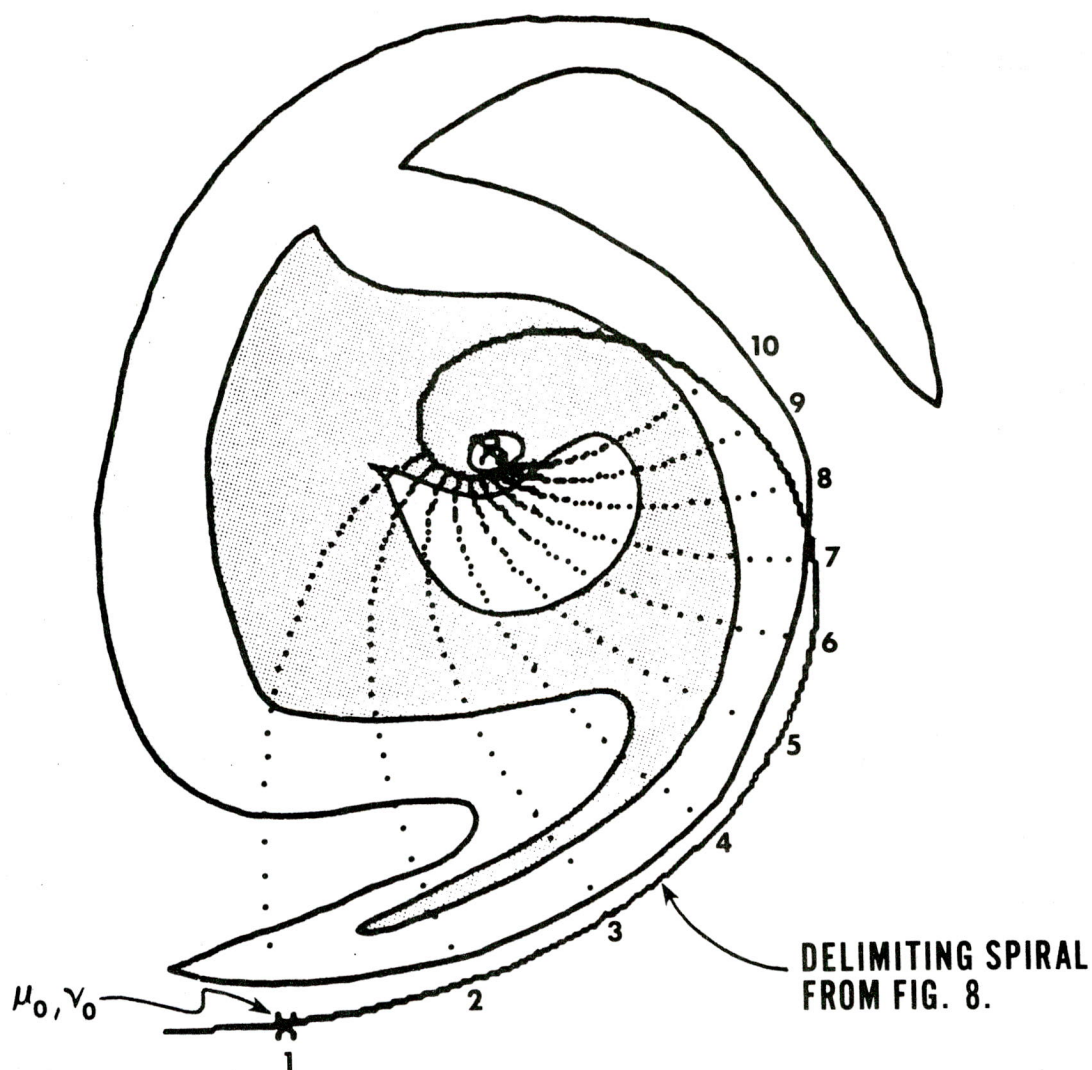


Figure 9. The spiral analysis grid for Fig. 8. The numbered dotted lines represent the ten spiral sections along which the spiral-Fourier analyses of the IR radiance field are taken. The dotted lines are orthogonal to the delimiting spiral and are composed of 40 equal spaced data points each. Note that the data points are not sampled until after each orthogonal spiral has passed over the delimiting spiral. This is necessary so that the same pixels are not sampled more than once.



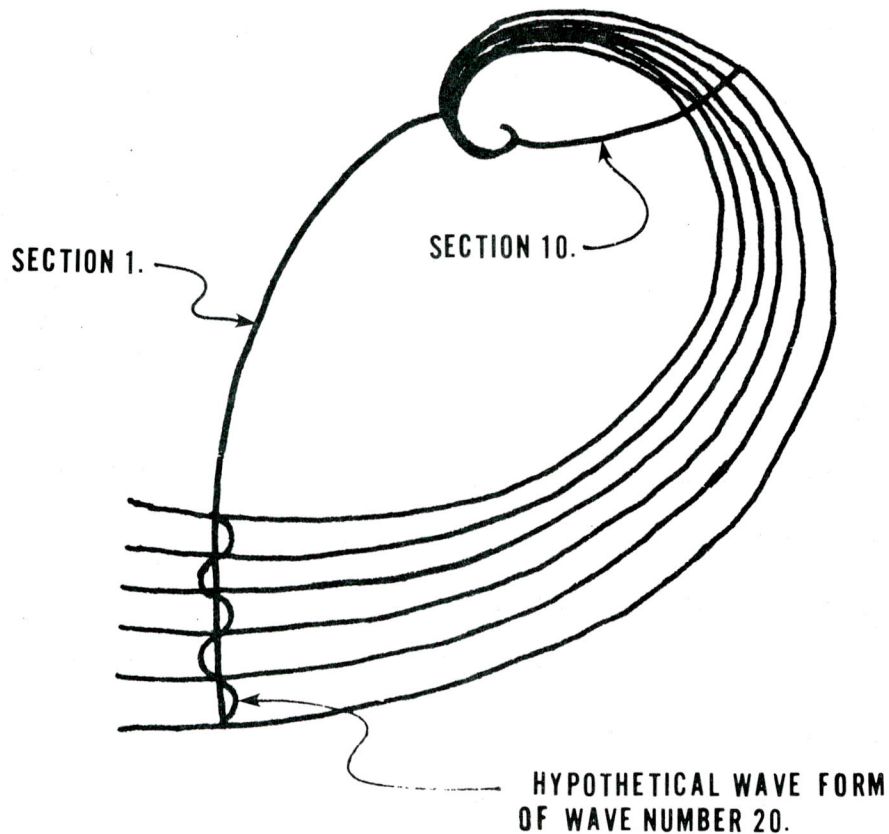


Figure 10. The parallel spirals show how the Fourier decomposition orthogonal to the delimiting spiral resolves spiral harmonics. The spirals shown are for wavenumber 20, which is represented in part by the sine wave. The actual analysis grid of Fig. 9 extends between the spiral sections 1 and 10.

Preliminary analyses showed that in some cases the variance was shifted artificially into the high wavenumbers. This was due to distortion (spikes) in the data: data sampled containing the radiance value of a point at the surface of the Earth (relatively warm) instead of that of a cloud top (relatively cold). Because of the nearly constant spectrum with respect to a large mean, the spikes constitute high frequency waves with large amplitudes that contribute to a large variance.

Ridding the data of large amplitude distortion is referred to as prewhitening since the ideal is to bring the spectrum close to that of white noise. According to Blackman and Tukey (1958) the flattening of the spectrum need not be precise since we need only to make the change of the power spectrum with frequency relatively small. The methodology developed for the present study to prewhiten the data is to identify the distortions in the data and set them equal to -1.5 standard deviations from the mean. A lower threshold IR value is calculated for each of the ten spiral sections<sup>2</sup> of the analysis using the above method, and the data prewhitened, prior to the Fourier analyses. Since only extremely low values of radiances are affected by this procedure, approximately 95% of the data are passed unaffected.

---

<sup>2</sup>The forty data points calculated for each orthogonal spiral are referred to as spiral sections or, if there is no ambiguity, simply as sections.

### 3.2 STATISTICAL ANALYSIS

Regression equations of the form

$$\hat{y} = a + b_1x_1 + b_2x_2 + \dots + b_px_p \quad (5)$$

are used to relate spiral parameters and past intensity measurements to current and future tropical cyclone intensity. The symbols are:

$\hat{y}$  are tropical cyclone intensity estimates at 0, 12, and 24 h from image time,

$x_1, \dots, x_p$  are the independent variables screened,

$b_1, \dots, b_p$  are the estimated coefficients,

$a$  is the estimated intercept, and

$p$  is the number of independent variables picked.

The hypothesis is that the intensity of tropical cyclones is related to their spiral banding structure as discussed in Chapter 2. In order to test this hypothesis, the past intensity measurements and the results of the spiral-Fourier analyses must be reduced to an appropriate field of potential predictors for the stepwise linear regression program.

#### 3.2.1 Selection of Potential Predictors

Dvorak (1975) has shown that persistence is an important predictor for tropical cyclone intensity. Therefore, tropical cyclone intensities 24 and 12 h before image time,

and their difference, are used as possible predictors (see Table 1). For the intensity forecast algorithms the intensity changes over the past 24 and 12 h using the estimated current intensity are calculated and used as possible predictors.

Swadley (1983) and Lahiri (1981) showed that the inflow angle ( $\alpha$ ) of the spiral cloud bands was also an important intensity predictor. To include the possibility of that relationship in this study,  $\alpha$  for the spiral analysis grid is also used as a potential predictor.

Table 1 also shows that additional potential predictors are considered. The position of the cyclone at image time is used to include possible latitudinal and longitudinal differences in intensity. Diurnal effects are parameterized using the image time and seasonal effects are parameterized using the Julian date of the image.

The large amount of data calculated using the spiral-Fourier analyses is reduced by limiting the contribution to the field of potential predictors to representations of the spiral signal and low wavenumber characteristics of the IR radiance field. This procedure is in agreement with the results of Black and Anthes (1971), Kurihara (1976), and Willoughby (1978) who showed that the spiral flow fields of tropical cyclones exhibit large signal to noise ratios for the low wavenumbers. As shown in Table 1, the potential predictors chosen to represent the low wavenumber



Table 1. Potential predictors

REPRESENTATION	DESCRIPTION
LOW WAVENUMBER CHARACTERISTICS	Number of harmonics necessary to explain 85% of the observed variance for sections 2,5,8, and the mean of all sections.
	Number of harmonics necessary to explain 90% of the observed variance for sections 2,5,8, and the mean of all sections.
	Number of harmonics necessary to explain 95% of the observed variance for sections 2,5,8, and the mean of all sections.
SPIRAL SIGNAL	Sum of the variance explained by the first three harmonics for sections 2,5,8, and the mean of all sections.
	Number of the harmonic explaining the maximum variance for sections 2,5,8, and the mean of all sections.
	Amplitude of the harmonic explaining the maximum variance for sections 2,5,8, and the mean of all sections.
VARIANCE	Total observed variance of sections 2,5,8, and the mean of all sections.
	Standard deviation of sections 2,5,8, and the mean of all sections.
	Threshold value of sections 2,5,8, and the mean of all sections.

Table 1. (CONTINUED)

REPRESENTATION	DESCRIPTION
PERSISTENCE	Intensity 24 h before image time.
	Intensity 12 h before image time.
	Intensity change from -24 h to -12 h before image time.
	Intensity change from -24 h to image time (using predicted current intensity).
	Intensity change from -12 h to image time (using predicted current intensity).
LOCATION	Sine of the latitude of the cyclone center at image time.
	Sine of the longitude of the cyclone center at image time.
SEASON	Julian date of satellite image converted to a sine wave and phase shifted to day 80.
DIURNAL EFFECTS	Image time converted to a sine wave and phase shifted to 0600 LST (local solar time).
SPIRAL GEOMETRY	Inflow angle of characteristic spiral analysis grid of the cyclone.

characteristics of the analysis are the sum of the variance explained by the first three harmonics, and the amplitude and number of the harmonic explaining the maximum amount of variance. As the explained variance spreads over the spectrum the spiral bands become less defined over the analysis grid and the signal to noise ratio is reduced. The potential predictors chosen to represent the spiral signal in the analysis are the number of harmonics necessary to explain 85%, 90%, and 95% of the observed variance of the IR radiance field.

Gentry et al. (1980) showed that measures of the variation of the IR radiance field were important for predicting tropical cyclone intensity. Therefore, the observed variance and the standard deviation of the IR radiance field are used as potential predictors; however, they are calculated from the prewhitened section values. To include a measure of the variation of the original field the threshold value used to prewhiten the data is also used as a potential predictor.

As seen in Table 1, the contribution of the results of the Fourier analyses to the field of potential predictors has been further reduced. Of the potential predictors described above, it was arbitrarily decided to use only their means over the ten sections and their values for sections #2, #5, and #8. Although this decision restricts the analysis, the computations are done more efficiently with

fewer potential predictors and the interpretation of the results is less complicated.

### 3.2.2 Calculation of Regression Equations

The stepwise multiple linear regression procedure used to relate the potential predictors to tropical cyclone intensity is the BMDP program P2R, revision 6-81 (Dixon, 1981). The program was developed at the Health Sciences Computing Facility, UCLA, under NIH Special Research Resources Grant RR-3. For all equations the F-method, forward stepping algorithm is used with a minimum F-to-enter value of 4.0, minimum F-to-remove of 3.9, and a tolerance of 0.05.

In the present study no variables are forced into the regression equations; all equations include intercepts, and no limit is set on the number of steps taken. The number of predictors is unrestricted. Further details of the calculation of multiple linear regression equations can be found in Dixon (1981) and Afifi and Azen (1979).

### 3.2.3 Independent Tests

The linear regression equations are then tested on an independent data set. The testing method used is to compare the independent data set to its estimate, calculated using the regression equations. The estimated and independent data sets are compared using the BMDP program 3D, revision 6-81 (Dixon, 1981). BMDP3D calculates the pooled Student's t-test for the difference between the means of



two groups, the Mahalanobis distance  $D^2$ , which is a measure of the distance between two groups, and Levene's F-test for equality of variances, an assumption of Student's t-test. Probability values are also calculated.

D square measures the distance between the means of two groups. It is defined as

$$D^2 = (\bar{Y} - \hat{\bar{Y}})^T S^{-1} (\bar{Y} - \hat{\bar{Y}}) \quad (6)$$

where  $(\bar{Y} - \hat{\bar{Y}})^T$  is the transpose of the matrix difference of the means of the independent measurements  $Y$  and the results of the regression of  $Y$  on  $X$ , denoted as  $\hat{\bar{Y}}$ .  $S$  is the covariance matrix of the two groups being compared. D square can be shown to have an F distribution and can, therefore, be assigned a probability value (p-value) based on an F distribution table with one degree of freedom (Afifi and Azen, 1979).

Student's t-test measures the difference between the means of the two groups and can also be assigned a p-value using a t distribution table with one degree of freedom. A critical assumption of the t-test is the equality of variances of the two groups. This assumption is tested by Levene's F-test which is a robust test performed by an analysis of variance on the absolute deviations of each case from its cell mean (Brown and Forsythe, 1974). F can be shown to have an F distribution and can, therefore, be

assigned a p-value using an F distribution table with one degree of freedom (Brown and Forsythe, 1974).

#### 4. DATA

The population from which the dependent and independent data sets were extracted consists of 97 digital IR satellite images of 15 tropical cyclones. All of the images are 2 n mi resolution in the spectral range of 10.5-12.6  $\mu\text{m}$  (thermal IR window). To ensure independent data, successive images are separated by at least 12 h (Gentry et al., 1980). From Table 2 we see that six tropical cyclones from the 1979 season, three East Pacific and three Atlantic, for a total of 76 images, comprise the dependent data set. Twenty-one images of nine tropical cyclones form the independent data set. Table 3 shows that the cyclones range from the 1979 to the 1983 season. Henri (1979) is the only Atlantic cyclone used in the independent data set.

In Tables 2 and 3 the image times are divided into 0000 and 1200 GMT. These synoptic times are only approximate image times, used to show the independency of the data.

##### 4.1 DEPENDENT DATA SET

###### 4.1.1 Satellite Imagery

The digital IR satellite data for 76 images processed with TEDS (Table 2) were acquired from GOES data tapes produced on the Off-line Data Ingest System (ODIS) by the Space Science and Engineering Center (SSEC), University of Wisconsin, Madison. These ODIS tapes can be acquired

Table 2. GOES 2 n mi resolution IR images used as the dependent data set in this study. The asterisks flag images where more than one spiral-Fourier decomposition was performed, therefore, more than one case was available per image.

1200 GMT					0000 GMT				
STORM NAME	DATE	POSITION		INTENSITY (KT)	STORM NAME	DATE	POSITION		INTENSITY (KT)
		LAT	LONG				LAT	LONG	
GLORIA	9/ 6/79	21.67	33.46	45.	GLORIA	9/ 7/79	23.24	36.50	45.
GLORIA	9/ 7/79	24.75	38.73	55.	GLORIA	9/ 8/79	25.96	39.61	55.
GLORIA	9/ 8/79	27.94	40.28	65.	GLORIA	9/ 9/79	28.82	41.12	65.
GLORIA	9/ 9/79	30.25	43.02	65.	GLORIA	9/10/79	31.72	44.55	65.
GLORIA	9/10/79	31.88	45.99	65.	GLORIA	9/11/79	31.05	46.97	59.
GLORIA	9/11/79	31.48	47.50	58.	GLORIA	9/12/79	32.15	48.40	63.
GLORIA	9/12/79	32.59	48.61	65.	GLORIA	9/14/79	36.42	42.38	84.
GLORIA	9/13/79	34.85	45.22	75.	GLORIA	9/14/79*	36.42	42.38	84.
GLORIA	9/14/79	39.75	38.28	86.	DAVID	8/26/79	11.80	40.50	20.
DAVID	8/26/79	11.60	44.00	37.	DAVID	8/27/79	11.70	46.40	50.
DAVID	8/27/79	11.76	49.86	68.	DAVID	8/28/79	11.97	52.89	98.
DAVID	8/27/79*	11.76	49.86	68.	DAVID	8/28/79*	13.70	58.27	123.
DAVID	8/28/79	12.80	55.77	127.	DAVID	8/30/79	15.50	61.98	123.
DAVID	8/29/79	14.77	60.42	119.	DAVID	8/31/79	16.81	67.33	130.
DAVID	8/30/79	16.17	64.95	129.	IGNACIO	10/24/79	11.90	96.70	25.
DAVID	8/31/79	17.29	69.33	130.	IGNACIO	10/25/79	11.52	99.32	35.
IGNACIO	10/24/79	12.80	93.40	30.	IGNACIO	10/26/79	13.00	102.00	40.
IGNACIO	10/25/79	12.16	100.83	40.	IGNACIO	10/27/79	15.90	105.20	70.
IGNACIO	10/26/79	14.10	103.10	55.	IGNACIO	10/28/79	17.42	108.16	121.
IGNACIO	10/27/79	16.80	105.30	90.	IGNACIO	10/29/79	18.20	109.00	90.
IGNACIO	10/28/79	17.04	108.37	113.	IGNACIO	10/30/79	18.10	105.00	55.
IGNACIO	10/29/79	18.10	107.90	70.	ENRIQUE	8/18/79	11.50	113.80	30.
ENRIQUE	8/18/79	12.00	116.10	30.	ENRIQUE	8/19/79	12.50	118.40	60.
ENRIQUE	8/19/79	13.20	121.80	65.	ENRIQUE	8/19/79*	12.50	118.40	60.
ENRIQUE	8/20/79	13.80	124.40	65.	ENRIQUE	8/20/79	13.40	123.00	70.
ENRIQUE	8/20/79*	13.80	124.40	65.	ENRIQUE	8/21/79	14.60	125.70	55.
ENRIQUE	8/21/79	16.00	125.00	55.	ENRIQUE	8/22/79	15.80	127.50	80.
ENRIQUE	8/22/79	18.20	128.80	120.	ENRIQUE	8/23/79	19.60	130.70	125.
ENRIQUE	8/23/79	20.20	132.00	75.	FREDERIC	9/ 1/79	12.38	45.78	50.
FREDERIC	8/31/79	12.09	43.26	45.	FREDERIC	9/ 2/79	13.57	51.59	63.
FREDERIC	9/ 1/79	12.95	48.56	58.	FREDERIC	9/ 3/79	16.05	59.22	65.
FREDERIC	9/ 2/79	14.31	55.73	55.	DOLORES	7/18/79	11.30	108.00	35.
FREDERIC	9/ 3/79	17.65	61.87	65.	DOLORES	7/19/79	12.70	113.80	65.
DOLORES	7/17/79	10.70	105.20	25.	DOLORES	7/20/79	13.90	116.60	75.
DOLORES	7/18/79	11.50	111.60	40.	DOLORES	7/21/79	16.80	118.80	95.
DOLORES	7/19/79	12.60	115.90	65.	DOLORES	7/22/79	20.20	122.10	65.
DOLORES	7/20/79	15.10	117.80	100.	DOLORES	7/23/79	24.20	124.80	30.
DOLORES	7/21/79	18.10	120.10	90.					
DOLORES	7/22/79	22.10	123.00	55.					



Table 3. Same as Table 2 except for the independent data set.

STORM NAME	DATE	0000 GMT		INTENSITY (KT)	STORM NAME	DATE	1200 GMT		INTENSITY (KT)
		LAT	LONG				LAT	LONG	
GILMA	7/30/82	14.90	129.50	107.	FABIO	7/21/82	19.10	116.50	46.
GILMA	7/30/82*	14.90	129.50	107.	ADOLF	5/24/83	12.30	104.30	100.
GILMA	7/27/82	10.20	119.00	44.	HENRI	9/17/79	20.80	94.00	72.
FABIO	7/21/82	16.20	113.00	61.	BARBARA	6/14/83	14.00	113.30	113.
FABIO	7/21/82*	16.20	113.00	61.	BARBARA	6/15/83	16.00	114.10	90.
DANIEL	7/14/82	17.30	126.00	72.	FEFA	8/21/79	14.80	104.50	40.
HENRI	9/17/79	20.00	93.20	53.	FEFA	8/22/79	16.50	111.00	90.
NORMAN	9/14/82	15.80	121.00	83.					
FEFA	8/22/79	15.80	108.00	60.					
FEFA	8/24/79	18.00	121.00	65.					
MIRIAM	9/ 1/82	14.80	118.00	65.					
MIRIAM	9/ 2/82	15.20	123.30	67.					
MIRIAM	9/ 2/82*	15.20	123.30	67.					
MIRIAM	9/ 3/82	16.00	129.00	75.					

through the National Environmental Satellite Data and Information Service (NESDIS), Washington, D.C.

The Pacific hurricanes were imaged with the GOES-3 satellite, stationed at 135 W and in a geosynchronous equatorial orbit at an altitude of approximately 35,800 km. GOES-3 was launched 16 June 1978 and became operational as GOES-WEST on 13 July 1978.

The IR images of the Atlantic hurricanes were taken by the SMS-2 satellite which was stationed at 75 W and operated as GOES-EAST. SMS-2 was also a geosynchronous satellite, capable of viewing the entire disk of the earth with each image. The radiometer used on both the GOES-3 and SMS-2 satellites was the Visible Infrared Spin Scan Radiometer (VISSR) which provided night/day observations of cloud cover and Earth/cloud radiance temperature measurements. SMS-2 was launched 6 February 1975 and became operational as GOES-EAST on 19 April 1979.

#### 4.1.2 Ground Truth Data

Individual descriptions of the life histories of the six tropical cyclones comprising the dependent data set (Table 2) are given in Appendix C. The positions at image times of Dolores, Enrique, and Ignacio are supplied by Gunther (1980), with the corresponding positions of the Atlantic hurricanes: David, Frederic, and Gloria supplied by Hebert (1980). Because some of the images used in this study were not taken at 0000 GMT or 1200 GMT, the positions

are interpolated between reports. The Akima (1970) interpolation method is used because it keeps the first derivative field continuous in the variable being analyzed, and is computationally efficient.

The intensities at image times are supplied by the Fleet Numerical Oceanography Center's archived tropical cyclone warning data file. Instead of analyzing the intensity of the non-standard timed images individually using the Dvorak technique, the Akima interpolation method is again used and rounded to the whole knot.

## 4.2 INDEPENDENT DATA SET

### 4.2.1 Satellite Imagery

The tropical cyclones making up the independent data set are listed in Table 3. The Atlantic hurricane (Henri) was imaged by the SMS-2 satellite and Fefa was imaged by GOES-3, both satellites described in 4.1.1. The images were acquired from NESDIS. The IR images of the 1982 season Pacific hurricanes were also taken by GOES-3. The IR images, however, were collected directly on NEPRF's GOES acquisition and data handling system (GADHS) by the SPADS Department.

The digital IR satellite images for the two 1983 season Eastern Pacific tropical cyclones were also collected directly by the SPADS Department. The cyclones were imaged by GOES-5, stationed at 75 W and operated as GOES-EAST. GOES-5 is a geosynchronous satellite but uses an upgraded

radiometer: VISSR Atmospheric Sounder (VAS). However, the upgrade applies to the sounding capabilities of the instrument, the IR images are still sensed with the VISSR. GOES-5 was launched in May 1981 and became operational as GOES-EAST on 5 August 1981.

#### 4.2.2 Ground Truth Data

The position at image times of Henri and Fefa are interpolated using the Akima (1970) method from Hebert (1980) and Gunther (1980), respectively. The positions and intensities for Adolf and Barbara, and the intensities for Henri and Fefa, are supplied by the Fleet Numerical Oceanography Center's archived tropical cyclone warning data file. The intensities at image times are interpolated between reports with Akima's method. The positions and intensities of the 1982 hurricanes are supplied by Emil Gunther of the Eastern Pacific Hurricane Center, Redwood City, and by Hans Rosendal, Central Hurricane Center, Honolulu, both by personal communication. The data provided are from post-analyzed best-track data sets. The data at image times are again interpolated between reports using Akima's method.

The data used to develop the 12 and 24 h intensity forecast regression equations and the independent data used for verification, are the best-track and warning intensities described above. Since the equations are neither developed nor verified using forecast data only 70 of the



76 images in the dependent data set can be used to develop the 24 h forecast regression equations. The last image of each cyclone has to be eliminated because of the lack of verification data. All images are available for use in the 0 and 12 h forecast equation development. Of the 21 independent cases Fefa, 24 August 1979, showed a strikingly rapid decay (80 kt over 36 h) which is not representative of either data set (mean 24 h change of 12 kt). For this reason Fefa, 24 August 1979, has been eliminated from the results.

Due to the small temporal range of images available for each tropical cyclone, individual descriptions are not given. Figure 11 is a plot of the frequency distribution for the current intensity (VMAX) for both data sets. The histograms are divided into Dvorak (1975) classifications, the T-number and associated wind speeds being the abscissa. Note the ordinate scale change. The bimodal distribution of the dependent data set is primarily due to the small sample size; however, the intensity data are not acquired from direct observations, they are estimated operationally using, primarily, the Dvorak (1975 and 1979) technique. Therefore, any operational bias in the issuance of intensity estimates will be reflected in the frequency distribution. Figure 12 is similar to Figure 11 except that it is for the intensity 12 h after image time (VP12). The plots

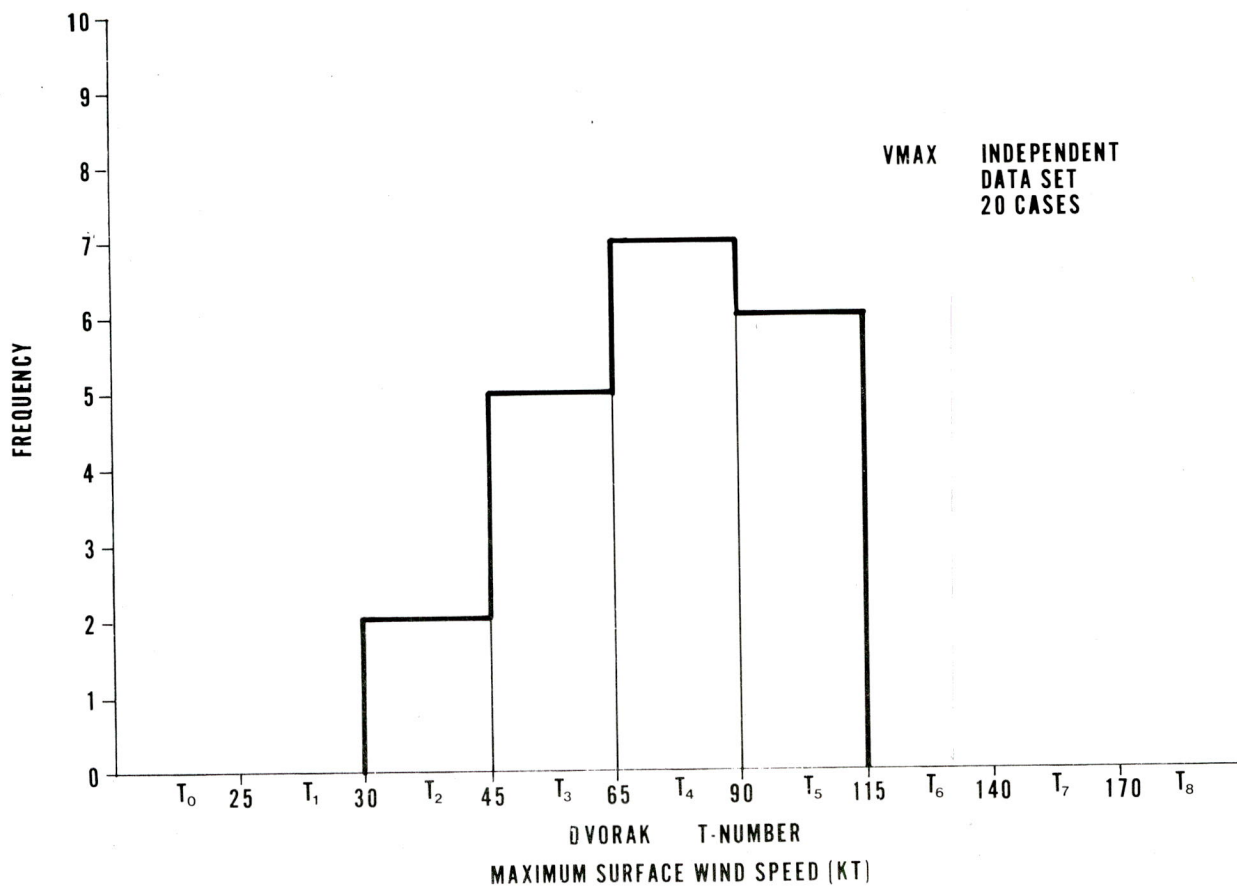
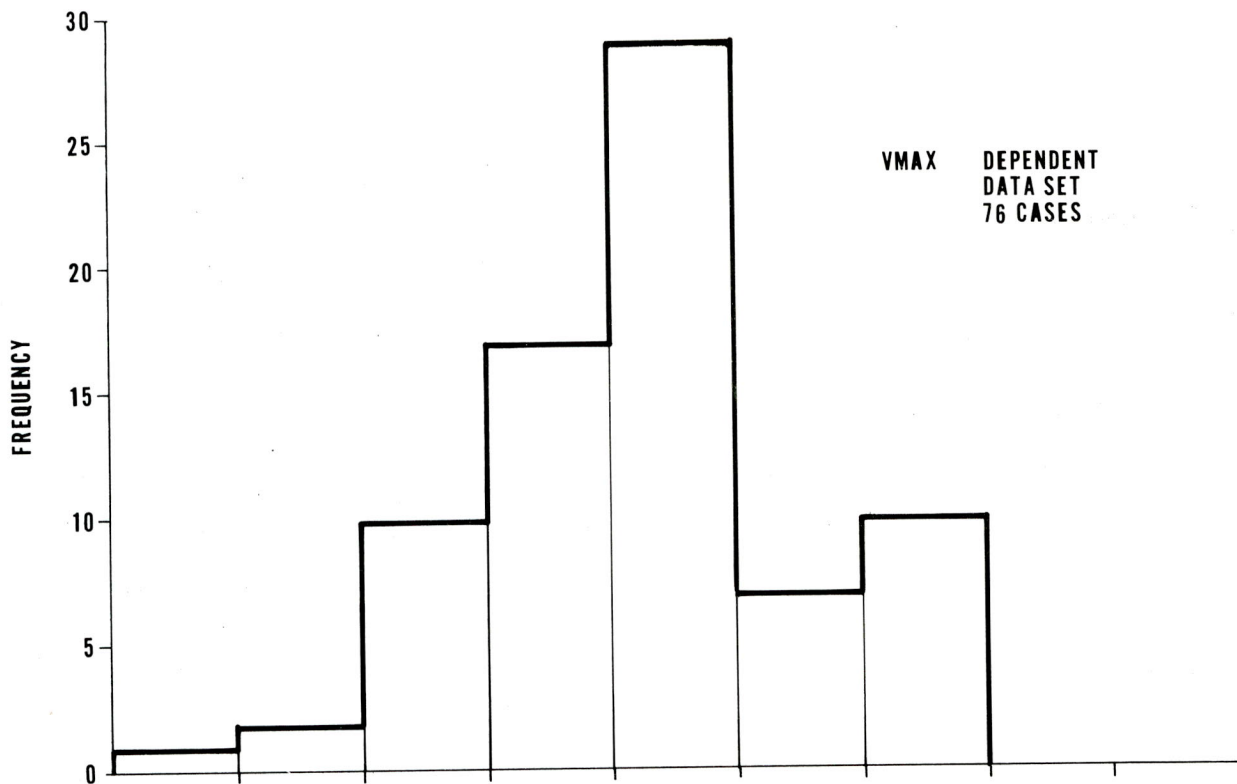


Figure 11. Frequency distributions of tropical cyclone intensity at image time (VMAX) for the dependent (top) and independent (bottom) data sets. Note the ordinate scale change. The stratification is by Dvorak T-number. The associated wind speed is in knots.

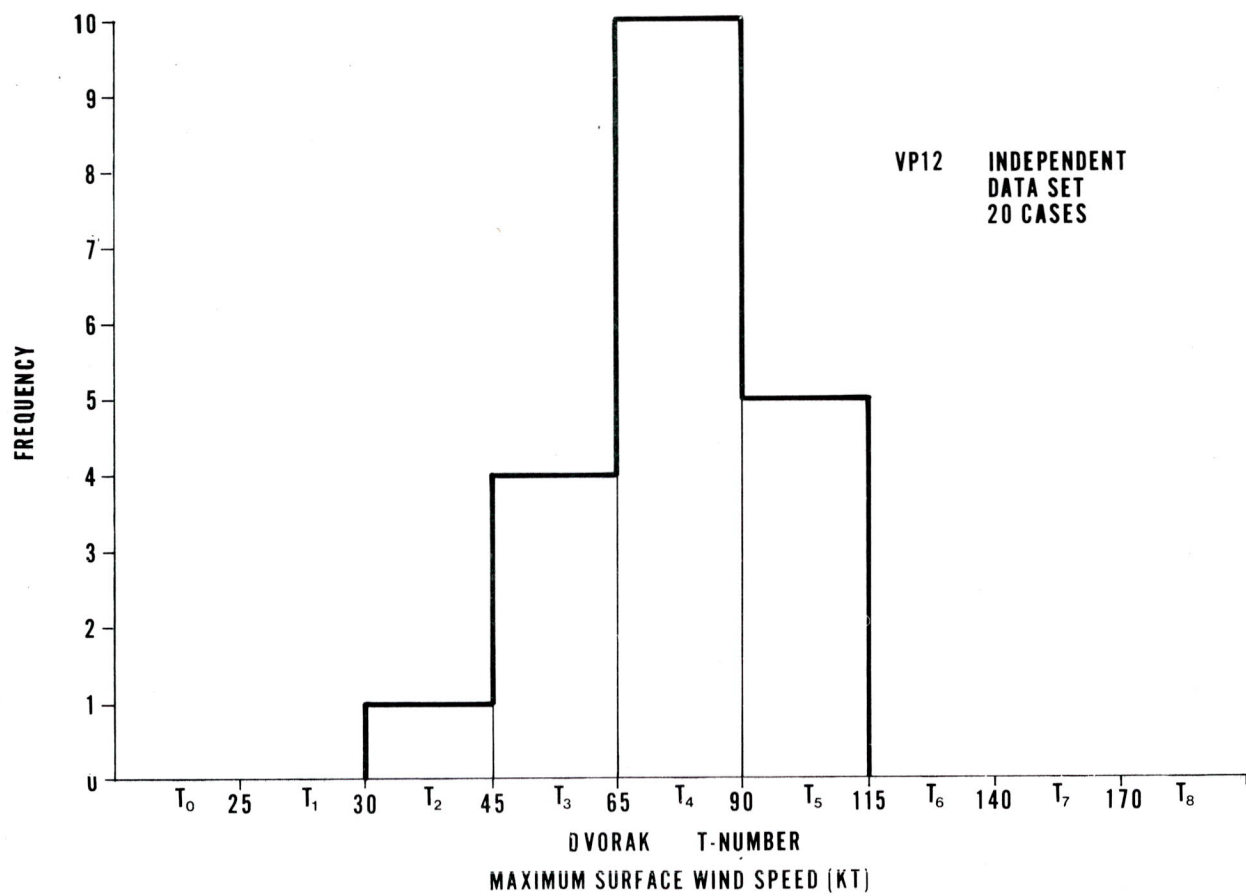
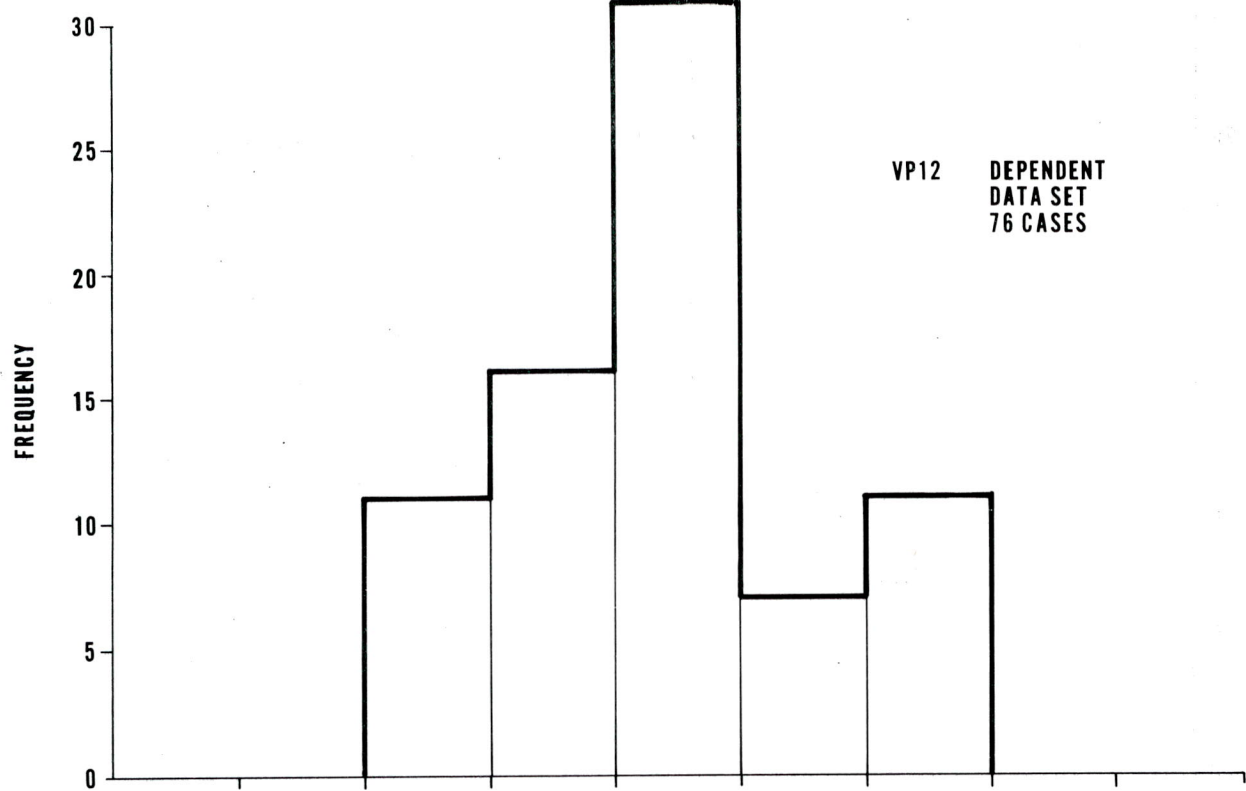


Figure 12. Same as Fig. 11 except for intensity 12 h after image time (VP12).

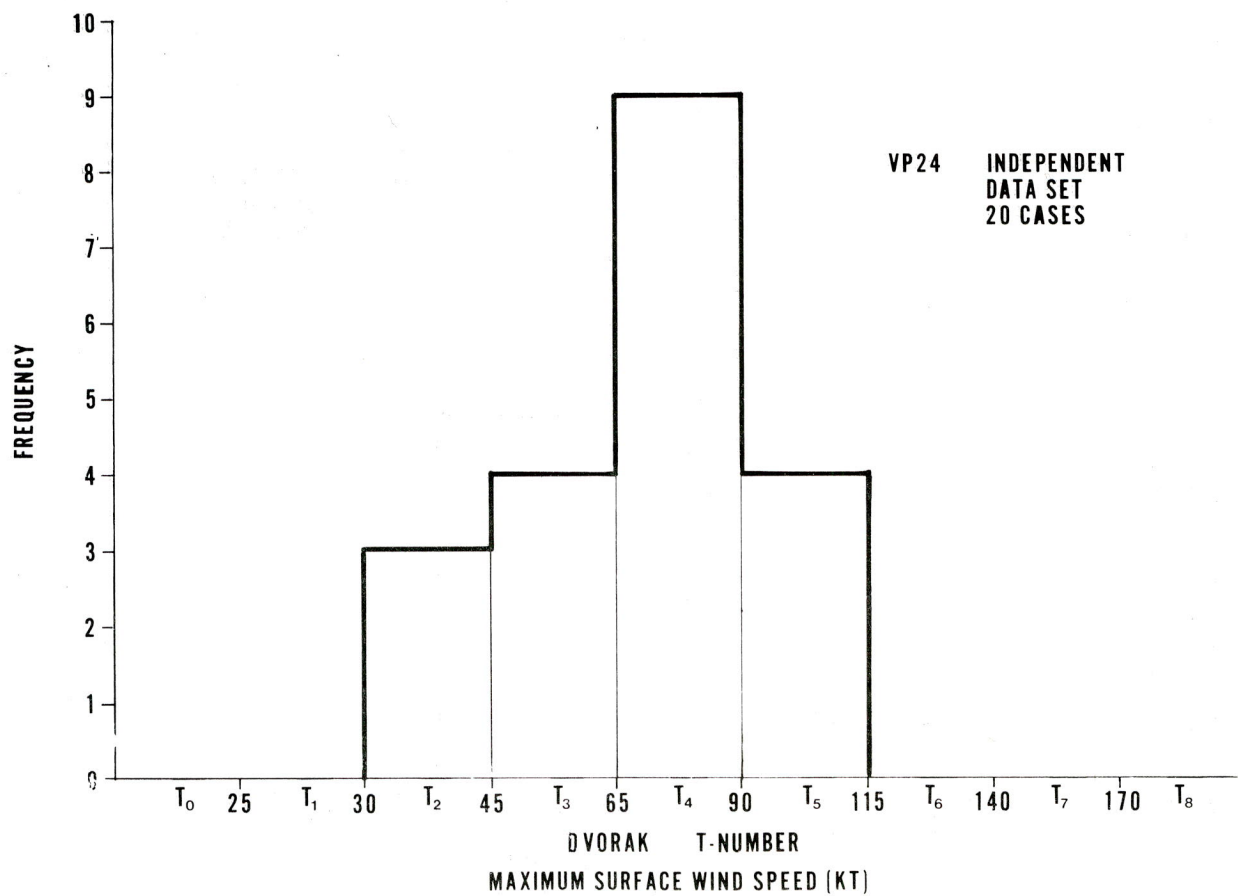
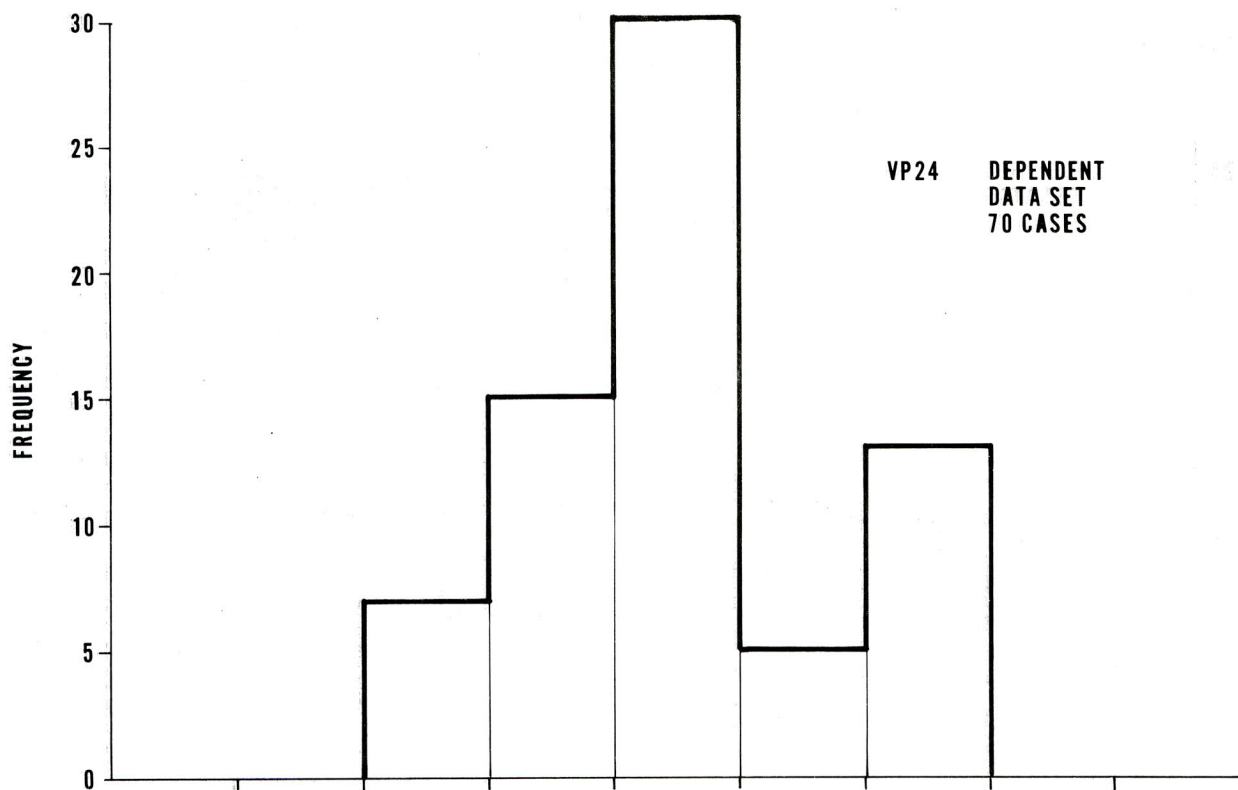


Figure 13. Same as Figs. 11 and 12 except for intensity 24 h after image time (VP24). Only 70 cases were available in the dependent data set.



show nearly the same distribution as VMAX except for an increase in the number of storms classified T4. Since most of the intensity monitoring techniques of 2.2 rely heavily on persistence, the temporal change of the frequency distributions are slow, as evidenced by the persistence of the bimodal distribution in the dependent data set. Figure 13 is similar to Figures 11 and 12 except for the change of variable to intensity 24 h after image time (VP24). Figure 13 shows nearly the same frequency distribution as Figure 12. Note that only 70 cases are represented by the dependent data set.

## 5. RESULTS

As described in 3.2.2, regression equations were developed to specify the current intensity (VMAX), and to make 12 h (VP12), and 24 h (VP24) intensity forecasts for tropical cyclones. Following Gentry et al. (1980) all of the cases were stratified into two groups depending upon whether or not the cyclone was of hurricane intensity 12 h before image time (VM12):  $VM12 \leq 65$  kt (LE65) and  $VM12 > 65$  kt (GT65). This stratification also ensured the availability of at least 23 cases per group for the development of each regression equation. The regression equations were developed for the three dependent variables using both the stratified and the unstratified data; therefore, the model consists of three equations for each dependent variable. One equation (ALL) was developed using all of the cases and can always be used to specify the variable. One of the two remaining equations (LE65 and GT65) can be used to again specify the variable depending upon VM12 as described above.

For the independent testing the results for each dependent variable using the LE65 and GT65 equations were combined to form the group GTLE65. Therefore, the estimates for each dependent variable form two groups: the group ALL, calculated using the ALL equation, and the group GTLE65, calculated using the LE65 and GT65 equations.

The independent test cases were also divided into the groups ALL, LE65, and GT65, and the recombination was performed the same as for the dependent data set. The stratification for the 20 case independent data set is nine cases LE65 and eleven cases GT65.

Table 4 is a list of the descriptions of the predictors picked by BMDP2R for the linear regression equations and the descriptions of the dependent variables. The predictors were selected from the field of potential predictors discussed in 3.2.1. Tables 5a and 5b are descriptive statistics for the predictors of Table 4. Table 5a represents the dependent data set and Table 5b represents the independent data set.

Comparing the two data sets, we find from the differences in the kurtosis that the dependent data has a higher probability of extreme values than the independent data set. The means of the variables agree quite closely except for the measurements of persistence (DVM12 and DV24) and ALFA. This implies the independent data set is comprised of tropical cyclones that, on the average, developed more rapidly than those making up the dependent data set. The mean of ALFA is  $7.5^\circ$  less for the more rapidly developing cyclones.

Comparing ALFA to Swadley's (1983) results, using the polar-log spiral equation but tracing spiral cloud bands, we find that the mean inflow angles ( $\sim 28^\circ$ ) are nearly

Table 4. Description of predictors selected by BMDP2R for the multiple linear regression equations and descriptions of the dependent variables.

NAME	DESCRIPTION
X90M	number of harmonics necessary to explain 90% of the observed variance for the mean of all sections
V32	percentage of the variance explained by the first three harmonics of section 2
HEMVM	number of the harmonic explaining the maximum variance for the mean of all sections
AMP8	amplitude (IR counts) of the harmonic explaining the maximum variance for section 8
AMPM	same as AMP8 except for the mean of all sections
TVAR5	total observed variance (IR counts) <sup>2</sup> for section 5
TVAR8	same as TVAR5 except for section 8
SD2	standard deviation (IR counts) of section 2
THLD8	threshold value (IR counts) of section 8
TIMES	image time normalized to 0600 LST and converted to a sine wave; $TIMES = \sin((2\pi/24)T)$ where $T = \text{MOD}(LT-6+24,24)$ and LT is the local solar time of the image
VM12	intensity (kt) 12 h before image time
DVM12	change in intensity (kt) between 24 and 12 h before image time; $DVM12 = VM12 - VM24$ where VM24 is the intensity 24 h before image time
DV24	change in intensity (kt) 24 h before image time using VMAX estimated by the appropriate regression equation; $DV24 = VMAX - VM24$
ALFA	inflow angle (degrees) of the characteristic spiral
VMAX	intensity (kt) at image time
VP24	intensity (kt) 24 h after image time
VP12	intensity (kt) 12 h after image time

} Dependent Variables



Table 5a. The mean, standard deviation, skewness, and kurtosis for all of the predictors picked by BMDP2R and the dependent variables. The variables are described in Table 4.

VARIABLE NAME	MEAN	STANDARD DEVIATION	SKEWNESS	KURTOSIS
X90M	6.447	1.670	.791	.219
V32	75.907	11.635	-.858	-.188
V3M	79.444	5.887	-.752	.314
HEMVM	1.195	.239	1.028	-.164
AMP8	211.964	16.039	-2.467	8.436
AMPM	209.362	15.465	-1.441	2.080
TVAR5	289.140	374.623	3.390	13.335
TVAR8	255.034	340.741	2.444	6.357
SD2	24.525	11.487	.287	-.737
THLDR	171.289	30.092	-.737	-.226
TIMES	.019	.421	-.146	-1.361
VM12	65.395	29.344	.641	-.273
DVM12	4.908	11.466	.472	1.403
DV24	9.210	11.251	-1.454	6.445
ALFA	28.364	9.388	.296	.085
VMAX	69.487	28.183	.634	-.217
VP24	75.286	27.467	.708	-.401
VP12	72.329	27.656	.681	-.331

Table 5b. Same as Table 5a except for the independent data set.

VARIABLE NAME	MEAN	STANDARD DEVIATION	SKEWNESS	KURTOSIS
X90M	6.935	1.661	1.213	1.658
V32	72.676	13.266	-.534	.028
V3M	76.494	7.669	-1.158	1.351
HEMVM	1.211	.324	1.403	.422
AMP8	213.466	8.200	.448	-.089
AMPM	210.700	5.900	-.664	-.956
TVAR5	289.179	264.633	1.284	.938
TVAR8	170.600	194.485	2.003	3.587
SD2	20.236	7.164	.400	-.773
THLDR	177.900	19.378	-.491	-.528
TIMES	.593	.453	-1.417	.845
VM12	67.250	23.420	.224	-.492
DVM12	8.300	12.215	.136	-.958
DV24	20.114	9.325	-.673	-1.045
ALFA	29.926	4.327	.300	-.656
VMAX	73.650	21.176	.321	-.906
VP24	68.250	18.487	-.222	-.813
VP12	72.800	15.917	-.202	-.728

equal. Therefore, the polar-log spiral representation of tropical cyclone cloud bands appears to be valid. This is expected since local polar coordinates are a good approximation to local spherical coordinates over the distance scales of a tropical cyclone.

#### 5.1 CURRENT INTENSITY (VMAX)

Results for current intensity (VMAX) from the stepwise multiple linear regression program BMDP2R and the results from the two groups comparison program BMDP3D are shown in Table 6a (ALL) and Table 6b (GTLE65). In these, and similar, tables the percentage of the variance explained by the regression equation (PVE) is the multiple correlation coefficient,  $R$ , squared and multiplied by one-hundred. The  $F$  ratio included in the analysis of variance (ANOVA) is a test of the significance of the coefficients of the predictors in the regression equations. The potential predictors are selected in such a manner as to maximize it. In general, the coefficients in the regression equations are significant at the 5% level and are listed in the equations from left to right in order of their relative significance.

The equations for ALL and GT65 show that persistence is a more important predictor for current intensity than are the spiral parameters; the average contribution to VMAX (ALL) from the predictor SD2 is a decrease in intensity of 5.5 kt and the GT65 equation contains only persistence. The estimation of the current intensity for tropical

Table 6a. Results of the regression, ANOVA, and comparison of two groups analyses for the group VMAX ALL.

EQUATION				
VMAX (ALL) = 21.78175 + 0.7911*VM12 + 0.54517*DVM12 - 0.27336*SD2				
-----				
MULTIPLE R			.97966	
MULTIPLE R-SQUARE			.95974	
STD. ERROR OF EST.			6.66785	
ANALYSIS OF VARIANCE				
	SUM OF SQUARES	DF	MEAN SQUARE	F RATIO
REGRESSION	8968.550	3.0	2989.517	67.240
RESIDUAL	711.364	16.0	44.460	
STATISTICS				
			P-VALUE	DF
MAHALANOBIS D SQUARE		.0002	.9618	1,38
T (POOLED)		-.05	.9618	1,38
F (FOR VARIANCES) LEVENE		.13	.7229	1,38

Table 6b. Same as Table 6a except for the group VMAX GTLE65.

EQUATION				
VMAX (LFF5) = -27.12597 + 0.87355*VM12 + 0.22718*AMPB + 6.72136*TIMES - 0.34092*ALFA				
VMAX (GT65) = 31.63646 + 0.62706*VM12 + 0.71402*DVM12				
-----				
MULTIPLE R			.94339	
MULTIPLE R-SQUARE			.89092	
STD. ERROR OF EST.			11.71577	
ANALYSIS OF VARIANCE				
	SUM OF SQUARES	DF	MEAN SQUARE	F RATIO
REGRESSION	8968.550	3.0	2989.517	21.780
RESIDUAL	2196.150	16.0	137.259	
STATISTICS				
			P-VALUE	DF
MAHALANOBIS D SQUARE		.0096	.7590	1,38
T (POOLED)		-.31	.7590	1,38
F (FOR VARIANCES) LEVENE		.03	.8707	1,38



cyclones below hurricane strength (LE65) depends on the cyclone's spiral geometry derived from the cloud bands, persistence, and image time. The inclusion of TIMES in the VMAX (LE65) equation suggests a diurnal variation in the current intensity of the weak storms. Browner et al. (1977) investigated the diurnal oscillation of the cirrus canopies of four tropical cyclones using satellite derived IR data, and found a negative correlation between storm intensity and the amplitude of the canopy oscillations. Thus, it appears that for weak storms the intensity and cloud top temperature are related on a diurnal scale.

The equations also show that a combination of persistence and spiral parameters is capable of explaining a large percentage of the variance of VMAX. The maximum PVE is 95% for ALL and the standard error (SDE) is 6 kt. The PVE for GTLE65 is 89% and the SDE is 12 kt. The PVE for both ALL and GTLE65 is larger than the 76% reported by Swadley (1983) for a 19 case dependent data set and using no persistence. Swadley presented no independent results. Both equations exceed the noise level of Dvorak current intensity estimates as reported by Erickson (1972) and Sheets and Grieman (1975). Erickson verified Dvorak estimates using aircraft reconnaissance data for 300 cases and reported a PVE of 78% and an RMS error (RMSE) of 15 kt. Sheets and Grieman verified 480 Dvorak estimates against the corresponding best-track data and found that 92% of the



estimates were correct to within one T-number and that the internal consistency of the technique between experienced analysts was 1.5 T-numbers.

Table 7 is a tabulation of all the independent results. Along the bottom are the means, standard deviations (STDV), total variances (TVAR), RMS errors, and PVE for the groups. The RMSE for ALL and for GTLE65 are both less than the RMSE reported by Erickson and the RSME for ALL is four knots smaller than Swadley's (1983) results. Figure 14 is a plot of the residuals of Table 7 against the estimated VMAX. The grouping in the higher wind speeds is an artifact of the Dvorak stratification in persistence for the predictors in the GT65 equation.

Returning to Tables 6a and 6b we find that the D square distances between the means of the estimates and observations are very small, and that the t-test for GTLE65 is six times that for ALL. The p-values confirm that we must accept the null hypothesis ( $H_0$ ) for both groups. In other words, the probability is 96% for ALL and 76% for GTLE65 that the two groups are members of the same population as VMAX. Although the Levene F-test has smaller p-values, we still cannot reject  $H_0$ .

From an F distribution table, we find that the F ratios for both ALL and GTLE65 are significant at the 1% level. This means that there is only one chance in

Table 7. Tabulated results of the regression analyses for VMAX, VP12, and VP24. Asterisk flagged images are the same as in Tables 2 and 3.

NAME	TIME	IMAGE	DATE	VMAX (KT)	ALL (KT)	GTLE65 (KT)	VP12 (KT)	ALL (KT)	GTLE65 (KT)	VP24 (KT)	ALL (KT)	GTLE65 (KT)
GILMA	2200 GMT	29 JULY	1982	107.00	110.40	115.76	82.00	102.38	88.72	53.00	94.57	128.17
GILMA	2200 GMT	29 JULY	1982*	107.00	109.48	115.75	82.00	95.90	116.56	53.00	89.76	91.32
GILMA	2300 GMT	26 JULY	1982	44.00	44.26	38.63	54.00	54.00	49.20	60.00	65.95	47.32
FABIO	2300 GMT	20 JULY	1982	61.00	66.60	70.17	51.00	72.04	66.31	41.00	79.04	119.43
FABIO	2300 GMT	20 JULY	1982*	61.00	65.58	70.17	51.00	69.94	75.52	41.00	72.92	92.22
FABIO	1700 GMT	21 JULY	1982	46.00	55.83	68.63	40.00	52.73	67.50	31.00	54.50	69.64
ADOLF	1600 GMT	24 MAY	1983	100.00	80.04	92.95	72.00	81.49	94.57	82.00	77.59	91.00
DANIEL	2200 GMT	13 JULY	1982	72.00	79.17	77.34	65.00	73.40	73.02	65.00	69.72	72.57
HENRI	2200 GMT	16 SEPTEMBER	1979	53.00	56.77	55.90	72.00	96.31	92.00	67.00	113.79	91.23
NORMAN	2000 GMT	13 SEPTEMBER	1982	82.00	78.58	82.92	30.00	78.68	59.74	89.00	77.17	62.10
HENRI	1000 GMT	17 SEPTEMBER	1979	72.00	63.23	60.66	67.00	65.48	65.74	53.00	69.36	87.13
BARBARA	1600 GMT	14 JUNE	1983	113.00	116.04	120.17	102.00	104.29	95.85	90.00	96.17	67.42
BARRAPA	1600 GMT	15 JUNE	1983	90.00	89.10	87.74	82.00	89.65	53.98	67.00	84.23	54.29
FEFA	1200 GMT	21 AUGUST	1979	40.00	34.86	35.76	60.00	67.31	63.39	90.00	89.82	54.14
FEFA	0000 GMT	22 AUGUST	1979	60.00	58.87	55.33	90.00	63.27	61.41	90.00	63.21	86.14
FEFA	1200 GMT	22 AUGUST	1979	90.00	76.89	62.27	90.00	73.47	65.31	100.00	73.54	89.64
MIRIAM	2200 GMT	31 AUGUST	1982	65.00	70.84	72.35	65.00	84.29	88.13	58.00	90.11	88.33
MIRIAM	2100 GMT	01 SEPTEMBER	1982	47.00	65.98	75.63	73.00	72.66	82.78	75.00	76.14	93.17
MIRIAM	2100 GMT	01 SEPTEMBER	1982*	67.00	69.39	75.88	73.00	63.19	74.97	75.00	62.37	84.12
MIRIAM	2100 GMT	02 SEPTEMBER	1982	75.00	72.58	81.70	75.00	75.61	108.17	75.00	75.92	94.94
MEAN				72.65	73.98	75.84	72.80	75.93	77.20	68.25	78.91	92.82
STANDARD DEVIATION				21.18	20.61	22.41	13.32	14.68	17.69	18.49	13.16	19.65
TOTAL VARIANCE				444.43	424.43	502.09	253.36	215.54	312.91	341.79	173.09	396.04
RMS ERROR					5.96	10.48		14.22	20.33		23.93	33.66
PERCENT VARIANCE EXPLAINED					95.97	89.09		60.70	30.60		20.20	26.57

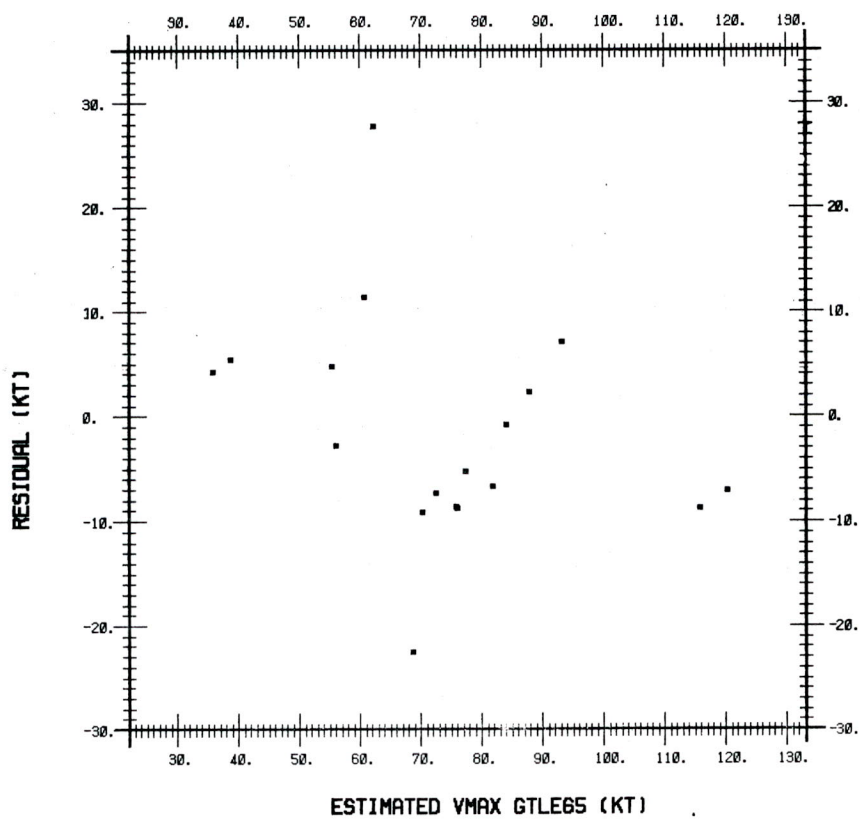
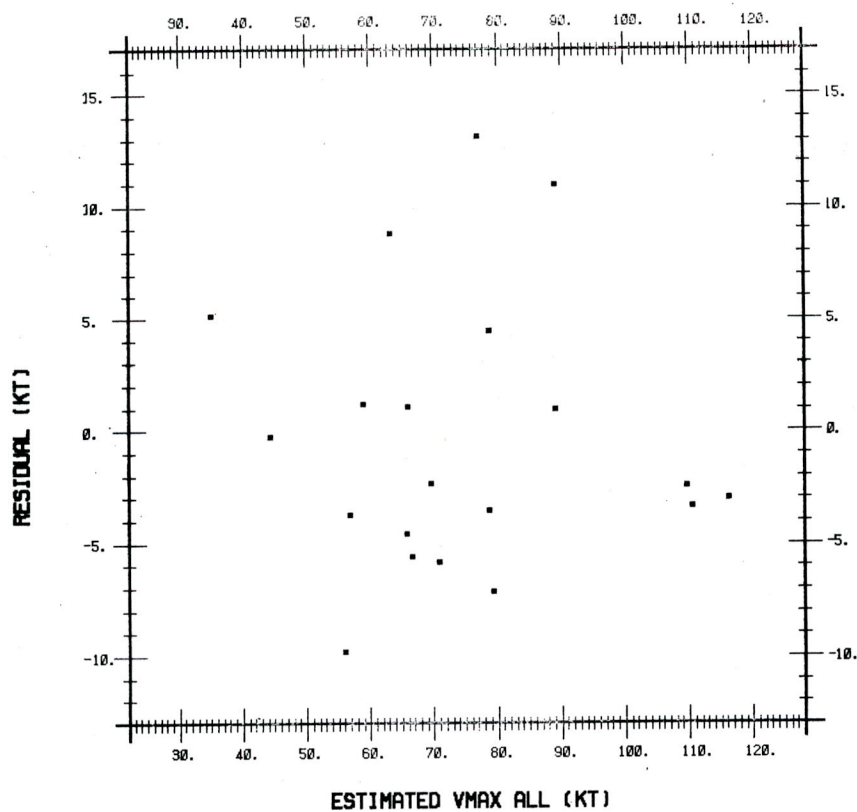


Figure 14. Residuals plotted against estimated VMAX ALL (top graph) and estimated VMAX GTLE65 (bottom graph). The residuals are given by  $Y - \hat{Y}$ .

one hundred that a random set of predictors could produce these results.

In summary, the results for VMAX show that a combination of persistence and spiral parameters is statistically significant in correctly estimating the current intensity of tropical cyclones. The errors in the model are at the noise level of the verification data, and are better than other published techniques.

## 5.2 12 h FORECAST INTENSITY (VP12)

Tables 8a and 8b show the results of BMDP2R and BMDP3D for VP12. Note VMAX in the regression equations are those estimated by the corresponding equations and groups for consistency. The results for the 12 h forecast data are not as impressive as those for the current intensity. The PVE for ALL (60%) is twice that for GTLE65. The standard errors are at the class limits for the larger T-numbers of the Dvorak classification scheme. This result is also indicated graphically from the contingency tables of Table 9. Considering total errors, GTLE65 performs better than ALL, ten errors to twelve, however, the number of two class errors is larger for GTLE65 (4) than for ALL (1), which means VP12 was correctly forecast by ALL 19 out of 20 times within one T-number category.

A skill score S is defined as

$$S = \frac{C - P}{T - P} \quad (7)$$



Table 8a. Same as Table 6a except for the group VP12 ALL.

EQUATION

VP12 (ALL) =  $-152.49974 + 0.75016 \cdot VMAX + 0.67883 \cdot AMPM + 21.14516 \cdot HEMVM + 0.01836 \cdot TVAR5$

MULTIPLE R .77908  
 MULTIPLE R-SQUARE .60697  
 STD. ERROR OF EST. 16.42223

ANALYSIS OF VARIANCE

	SUM OF SQUARES	DF	MEAN SQUARE	F RATIO
REGRESSION	5067.200	4.0	1266.800	4.697
RESIDUAL	4045.346	15.0	269.690	

STATISTICS

		P-VALUE	DF
MAHALANOBIS D SQUARE	.0691	.4110	1,38
T (POOLED)	-.83	.4110	1,38
F (FOR VARIANCES) LEVENE	.13	.7174	1,38

Table 8b. Same as Table 6a except for the group VP12 GTLE65.

EQUATION

VP12 (LE65) =  $-130.33819 + 0.98525 \cdot VMAX + 0.52087 \cdot AMPM + 21.26324 \cdot HEMVM + 0.01355 \cdot TVAR5$

VP12 (GT65) =  $-217.34952 + 0.58226 \cdot VMAX + 0.07098 \cdot TVAR8 + 1.36664 \cdot THLD8$

MULTIPLE R .55315  
 MULTIPLE R-SQUARE .30597  
 STD. ERROR OF EST. 23.09397

ANALYSIS OF VARIANCE

	SUM OF SQUARES	DF	MEAN SQUARE	F RATIO
REGRESSION	5067.200	3.5	1447.771	2.715
RESIDUAL	8266.639	15.5	533.332	

STATISTICS

		P-VALUE	DF
MAHALANOBIS D SQUARE	.0650	.4252	1,38
T (POOLED)	-.81	.4252	1,38
F (FOR VARIANCES) LEVENE	.45	.5073	1,38

Table 9. Contingency tables for VP12 ALL (left) and VP12 GTLE65 (right) classified by the Dvorak (1975) scheme. The values in the tables are category counts.

OBSERVED VP12										OBSERVED VP12									
Forecast (All)		0	1	2	3	4	5	6	Total	Forecast (GTLE65)		0	1	2	3	4	5	6	Total
0										0									
1										1									
2										2									
3										3									
4										4									
5										5									
6										6									
TOTAL		1	4	10	5				20	TOTAL		1	4	10	5				20

where  $P$  is the number of correct forecasts by persistence,  $C$  is the number of correct forecasts by the model, and  $T$  is the total number of forecasts. The  $S$  for ALL is  $-0.33$  and the  $S$  for GTLE65 is  $-0.11$ . These results indicate the models are not skillful in predicting VP12 within the correct Dvorak T-number category when compared to persistence. These results cannot be compared because there are no published 12 h forecast tropical cyclone intensity error statistics.

From Table 7 we find that the RMSE for ALL is 14 kt, one-third better than the RMSE for GTLE65. This is not reflected in the skill score. The residuals are plotted against the predicted VP12 in Figure 15. The results show a randomness that is usually associated with an adequate model (Afifi and Azen, 1979).

From Table 8a we find that the  $F$  ratio for ALL is significant at the 5% level. The  $F$  ratios are an order of magnitude less than those for VMAX, but the  $p$ -values still require that we accept  $H_0$ ; the two groups are most likely from the same population as VP12.

From Table 7 we can see that the difference between the means is larger for GTLE65 than it is for ALL. This 4 kt bias in the model is due to the difference between the mean rate of intensity change between the dependent and independent data sets, discussed earlier in this chapter,

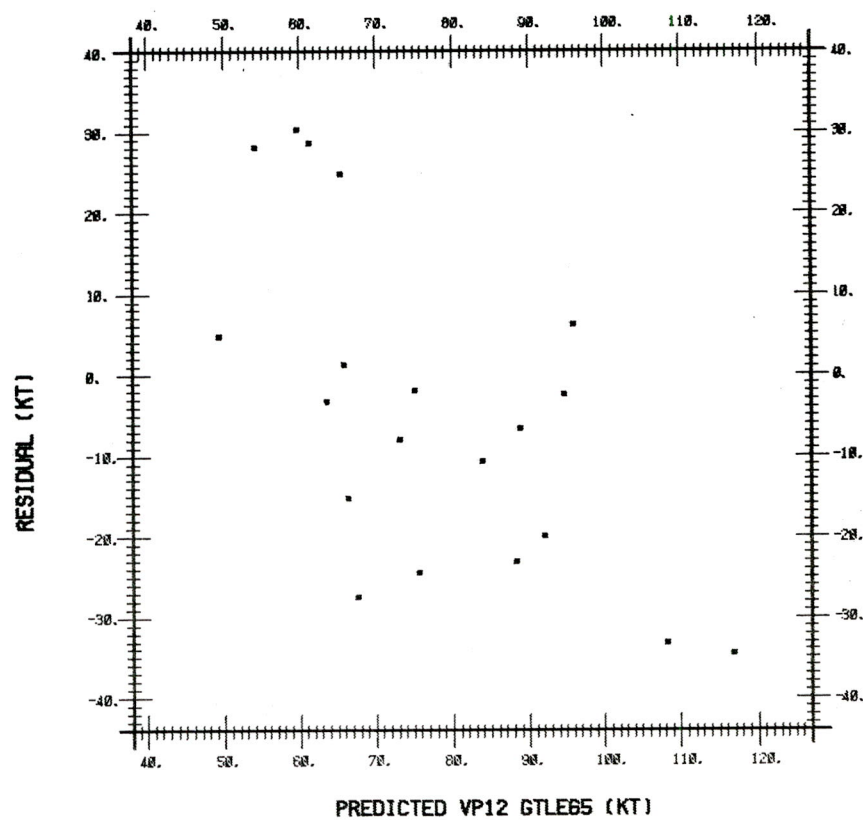
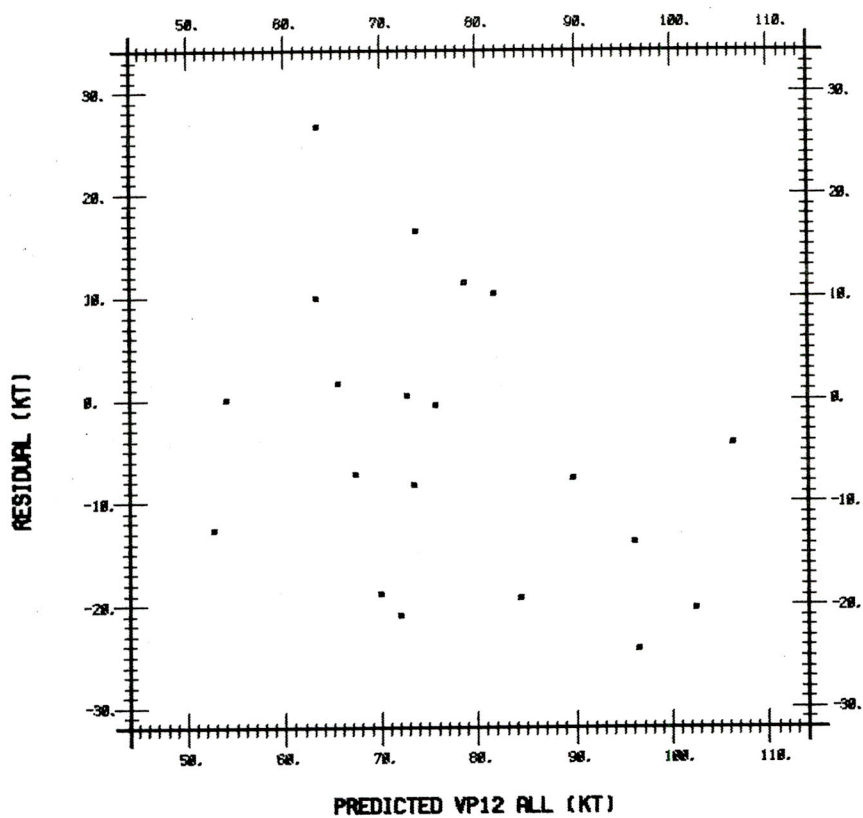


Figure 15. Same as Fig. 14 except for the population VP12.



and should only be removed after testing the model on a larger independent data set.

It is interesting to note that the form of the equations for ALL and LE65 is the same; this is carried through to VP24 (ALL), discussed next. This reflects the consistency of the spiral representation of the banding structure of the tropical cyclone and validates the credibility of the model.

### 5.3 24 h FORECAST INTENSITY (VP24)

The results of the regression analyses and the independent test for VP24 are shown in Tables 10a and 10b. The form of the regression equation for ALL was mentioned previously. A reason that this form of equation persists is that the Fourier analyses always include the coldest cloud tops. Gentry et al. (1980) showed that a 333 km radial ring about the storm center enclosed the area of coldest cloud tops, the overshooting convection in and around the eye wall. Gentry et al. also showed the average cloud top temperature for the radial ring to be a significant predictor for 24 h intensity forecasts. This importance is indicated in the present study by the persistence in the equations of the number and amplitude of the harmonic explaining the maximum variance for the mean of all sections. These predictors suggest the importance of the high IR values of the coldest cloud tops as intensity predictors.

Table 10a. Same as Table 6a except for VP24 ALL.

EQUATION

VP24 (ALL) = -204.98015 + 0.48984\*VMAX + 0.96028\*AMPM + 32.69795\*HEMVM + 0.01992\*TVAR5

MULTIPLE R .44945  
MULTIPLE R-SQUARE .20201  
STD. ERROR OF EST. 26.59049

ANALYSIS OF VARIANCE

	SUM OF SQUARES	DF	MEAN SQUARE	F RATIO
REGRESSION	6835.750	4.0	1708.938	2.417
RESIDUAL	10605.813	15.0	707.054	

STATISTICS

		P-VALUE	DF
MAHALANOBIS D SQUARE	.4195	.0475	1,38
T (POOLED)	-2.05	.0475	1,38
F (FOR VARIANCES) LEVENE	2.59	.1159	1,38

Table 10b. Same as Table 6a except for VP24 GTLE65.

EQUATION

VP24 (LE65) = -10.71321 + 0.72176\*VMAX + 0.7413\*DV24 + 0.47904\*V32

VP24 (GT65) = 29.51729 + 2.54618\*AMPM - 10.88206\*X90M - 5.17114\*V3M

MULTIPLE R .51542  
MULTIPLE R-SQUARE .26566  
STD. ERROR OF EST. 37.63501

ANALYSIS OF VARIANCE

	SUM OF SQUARES	DF	MEAN SQUARE	F RATIO
REGRESSION	6835.750	3.0	2278.583	1.609
RESIDUAL	22662.299	16.0	1416.394	

STATISTICS

		P-VALUE	DF
MAHALANOBIS D SQUARE	.5541	.0238	1,38
T (POOLED)	-2.35	.0238	1,38
F (FOR VARIANCES) LEVENE	0.00	.9995	1,38

This agrees with a conclusion of Swadley (1983), who found the maximum IR value of the coldest cloud top to be a significant predictor of tropical cyclone current intensity.

The equation for GT65 is interesting because it is composed only of spiral parameters. Persistence is found not to be a significant predictor for 24 h forecasts of intense tropical cyclone maximum wind speed. This agrees with the results of Sheets and Grieman (1975) who found that the Dvorak forecasting method (which relies highly on persistence) works worst for intense storms.

The PVE for ALL is 20% and for GTLE65 is 26%, and is much less than that explained at 12 h. From Table 11 we find that the number of class errors larger than one is greater for GTLE65, indicating a better forecast by ALL when compared to persistence, even though ALL has a lower PVE. This result is also evident in the skill score, which is 0.08 for ALL and -0.33 for GTLE65. The prediction for VP24 made by using the ALL equation is the only forecast more skillful than persistence.

From Tables 10a and 10b, we see that the SDE for ALL is 26 kt and the SDE for GTLE65 is 37 kt, much greater than one Dvorak T-number interval. The statistics for the analysis of the two groups show that the p-values for the pooled Student's t-test and D square are low enough to reject  $H_0$ . At the 4% level for ALL and at the 2% level for GTLE65 we must peremptorily assume that the two groups are not from

Table 11. Same as Table 9 except for the population VP24.

OBSERVED VP24										OBSERVED VP24									
Forecast (All)		0	1	2	3	4	5	6	Total	Forecast (GTLE65)		0	1	2	3	4	5	6	Total
T		0								T		0							
N		1								N		1							
U		2								U		2							
M		3			1				1	M		3			1	2	1		4
B		4		2	3	7	2		14	B		4		1	2	3	3		9
E		5			1	1	2		4	E		5		1		4			5
R		6				1			1	R		6			1	1			2
TOTAL			3	4	4	9	4		20	TOTAL			3	4	9	4			20



the same population as VP24. The results indicate that these regression equations have no usefulness as forecast aids.

In a verification of the Dvorak (1975) forecast method against aircraft reconnaissance data, Erickson (1972) found that the 24 h forecast technique explained 31% of the variance over 178 observations. This implies that the noise level of the Dvorak forecasting method is near the skill level of the objective forecast method presented. These results are similar to those of Sheets and Grieman (1975) who found that the 24 h forecast errors of the Dvorak method were of the same magnitude as the errors made by forecasts using climatology. Shewchuk and Weir (1980) showed that the mean error for the Dvorak (1979) forecasting method over 400 cases was 8 kt when verified against best-track data. Their results are similar to the errors for 24 h intensity forecasts made by using the objective technique described by Gentry et al. (1980). Their 24 h forecast mean absolute error was reported as 14 kt, which, from Table 7, compares to RMS errors of 23 kt for ALL and 33 kt for GTLE65. The results presented above indicate that the 24 h objective forecast technique presented in this study is not as skillful as the other satellite-based tropical cyclone forecasting techniques in the literature.

We can also see from Table 7 that ALL can only reproduce about one-half of the total variance observed, while

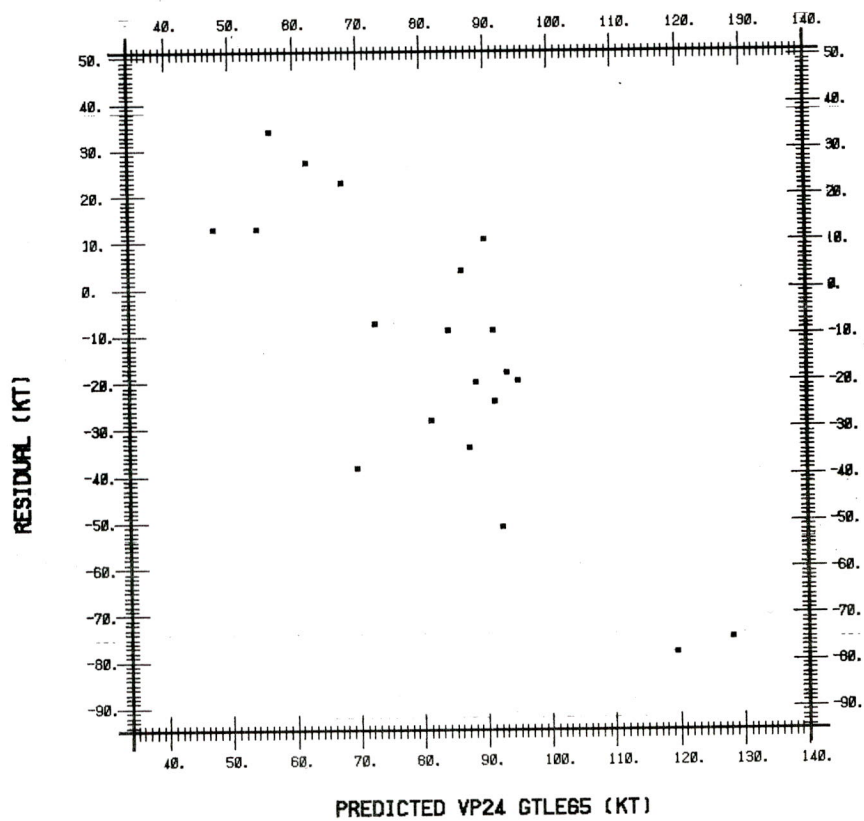
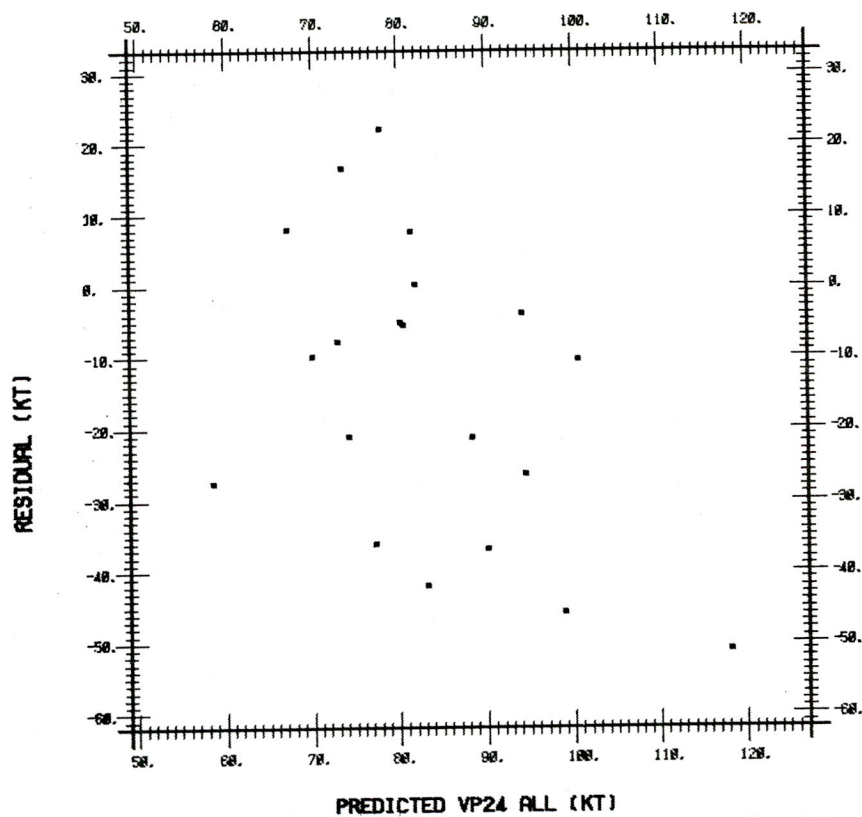


Figure 16. Same as Fig. 14 except for the population VP24.

the TVAR of GTLE65 is very close to that observed for the tropical cyclones. The poor results shown by PVE and RMSE are partly due to the differences between the means of the groups. The bias in ALL of +10 kt and in GTLE65 of +14 kt are close to the bias of +11 kt Gentry et al. (1980) found in their results. The biases are evident in the large number of negative residuals, graphed in Figure 16 against the forecasts for VP24. The bias is particularly evident for the large values in GTLE65. The bias in the forecast is too large to be attributed solely to differences between the data sets as it was for VP12. The results indicate that other factors relating to tropical cyclone intensity have to be taken into account in order to develop better 24 h predictive techniques (Afifi and Azen, 1979). With a limited data set further conclusions about the cause of the bias are not possible.

## 6. CONCLUSIONS AND RECOMMENDATIONS

### 6.1 CONCLUSIONS

The objective of this study was to determine a quantitative relationship between satellite measurements of the IR radiance field and the intensity of tropical cyclones. A spiral analysis technique was used to quantify the spiral patterns of the cloud bands in the IR data and multiple linear regression techniques were used to relate the derived spiral parameters to tropical cyclone intensity. The results presented validate the hypothesis that the spiral structure of cloud bands associated with tropical cyclones can be characterized by fitting spherical-log spirals to the IR radiance field of their cloud tops; however, the polar-log spiral representation of cloud spirals used by other researchers appears to be valid for tropical cyclones located near the satellite sub-point.

The regression equations developed show significant skill in estimating current tropical cyclone intensity and in making 12 h intensity forecasts. This nowcasting skill is unique because the technique presented is a stand-alone objective analysis and forecast method. The only input is a current IR image and the tropical cyclone's intensity for the previous 12 and 24 h.

There is a positive bias in the forecasted intensities that is similar to the bias found by Gentry et al. (1980).



This suggests that other variables not considered here are necessary to correctly predict tropical cyclone intensity or that the IR radiance field's signal to noise ratio is too low for the signal to be properly detected.

The predictors that occur most frequently in the regression equations are related to the maximum IR count found in the central dense overcast area around the center of tropical cyclones. This result was also found by Swadley (1983) to be important for current intensity estimates, and by Gentry et al. (1980) to be important for intensity forecasts.

A negative result regarding predictive skill was found for the variable ALFA, the inflow angle of the characteristic spherical-log spiral analysis grid for the tropical cyclone. This supports the findings of Peterson et al. (1983) and contradicts the findings of Lahiri (1981) and Swadley (1983).

## 6.2 RECOMMENDATIONS FOR FUTURE WORK

The results presented above demonstrate that more research needs to be undertaken in the area of satellite derived tropical cyclone intensity estimates and forecasts.

A natural expansion of this study would include other large scale potential predictors available on an IR image. Some examples of additional potential predictors are the size of the cyclone measured along and perpendicular to a

set of predetermined axes; the areal extent of a certain equivalent blackbody cloud top temperature corrected for diurnal oscillations using the results of Browner's et al. (1977) study; the width and azimuthal extent of large cloud bands using methods developed by Dvorak (1975, 1979); and sea surface temperatures in the cloud free areas around the cyclone which are important for longer range forecasts. In addition, one could include more of the cloud covered area in the analysis grid. A typical spiral grid used in this study covered only about one-third of the cloud field of the tropical cyclone.

A fitted spiral with a variable offset radius could be added to TEDS in order to more accurately determine the spiral characteristics of the cloud bands. Energy considerations constrain the radial inflow so the inflowing air cannot penetrate to the geometric center of the storm. At a typical distance of 10 to 100 km, the air turns upward in a ring of convection called the eye wall; and here is where the strongest wind speeds typically occur (Anthes, 1982). This radius of maximum wind speed is an important parameter to be able to predict, and its correlation with the offset radius should be investigated. In addition, the behavior of the spiral energy spectrum should be investigated.

This study concentrates on information available from IR images of tropical cyclones, consequently, the cloud bands analyzed are composed of the coldest, upper-level

clouds discernible on an image. But the widely used Dvorak (1975) method for estimating tropical cyclone intensity relies on visible imagery for the spiral analysis of low-level cloud bands. TEDS also has the capability of fitting spherical-log spirals to cloud bands on visible images; IR images are only necessary for the quantitative data to be Fourier decomposed. This capability could be exploited by analyzing image pairs: visible and IR images temporally spaced no further than thirty minutes apart. This idea could be expanded further by analyzing image sets and including the temporal changes of the spiral parameters as potential predictors.

Finally, both the dependent and independent data sets should be expanded from their sizes in the present study. More significance could, therefore, be placed on the statistical arguments.

APPENDIX A

TEDS SOFTWARE DOCUMENTATION

Figure A1 is the functional flow diagram for the TEDS program. The FORTRAN codes for the subroutines SPIREL and STAN are reproduced in this appendix because they are the important analysis routines written specifically for use in this study. SPIREL contains the spherical-log spiral curve fitting algorithm and STAN produces the spiral analysis grid and calls the Fourier analysis subroutine used to quantify the spiral patterns of the cloud bands.



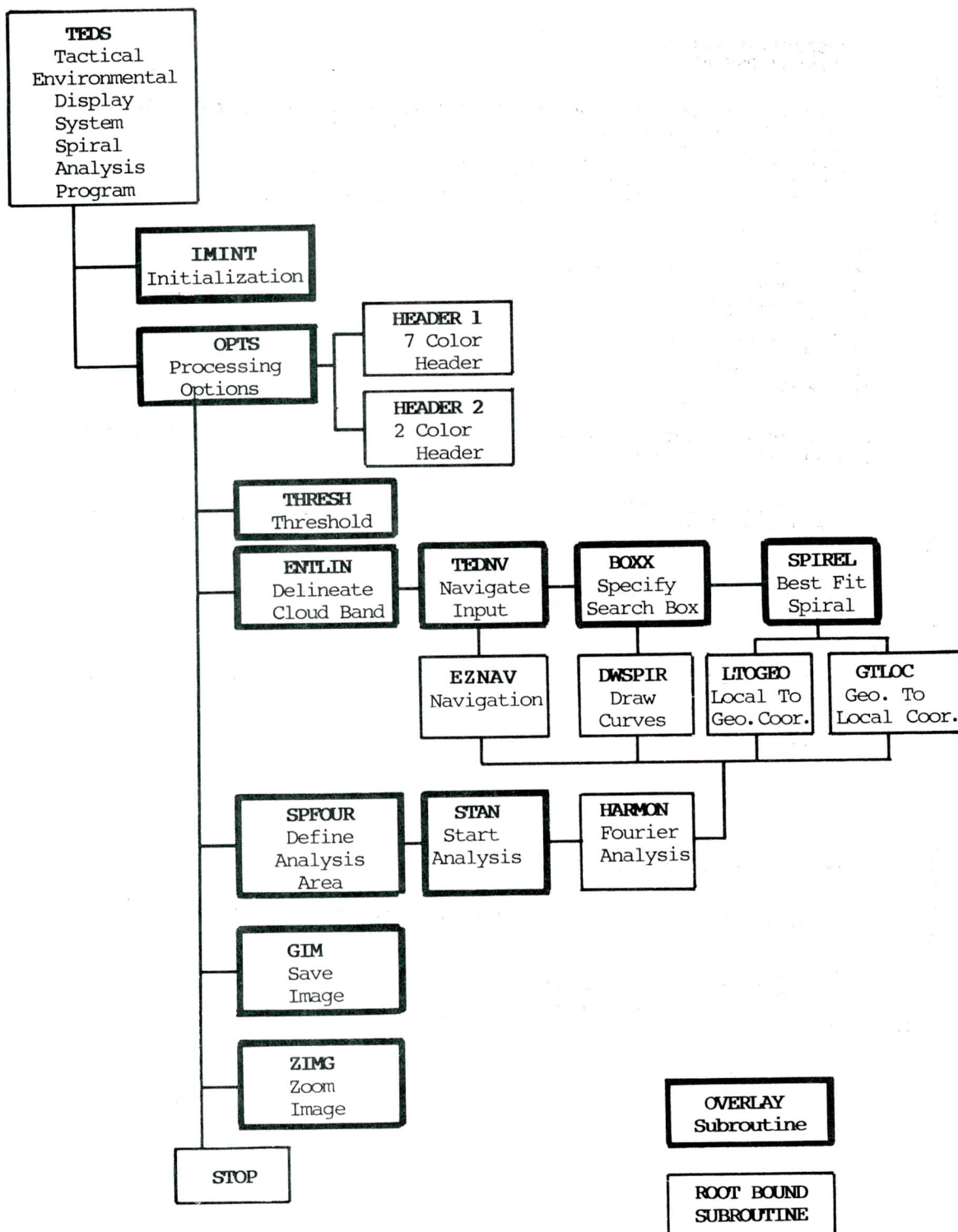


Figure A1. Functional flow diagram for the TEDS program.  
The program flow is down the page, with horizontal excursions where indicated.

```

SUBROUTINE SPIREL
OVERLAY OSPIREL

COMMON/SCAT/ ICAT(256),PHIX(100),A(100),B(40),C(40),D(40),E(80)
COMMON/BUFR2/ JOB,IFILL(256),IB(256),NAME1(10)
COMMON/GF/ IBUF(256)
COMMON/SPLOC/ NOPTS,XLON(40),PHI(40),XW1,XE1,YN,YS
COMMON/SV/ IFLAG,IHEM,PHIS(20),XLAMS(20),COTALS(20)
COMMON/BUFR1/ IER,IERR,ILINE(256),IOPT,NTYPE

REAL NUP, NUOP
REAL NUMIN
REAL LAMBDA(100),MUEX,NUEX
REAL LAMBDA(40)
REAL MU0, NU0
REAL MUO(40),NUO(40),AMU(40)
REAL NUMAX
REAL MUSUM,MUOP
REAL MUAV
REAL NUE, LAMBDA(100)

EQUIVALENCE (XLON(1),LAMBDA(1)),(LAMBDA(1),A(1)),(MUO(1),B(1)),(NUO(1),C(1))
EQUIVALENCE (AMU(1),D(1))

PI = 3.1415926535898
DTR = 0.0174533 ;DEGREES TO RADIAN

TYPE
TYPE"WAIT.....CALCULATIONS IN PROGRESS"
TYPE

DO 11 I=1,40
MUO(I) = 0.0
NUO(I) = 0.0
AMU(I) = 0.0
CONTINUE

11

XNOPTS = FLOAT(NOPTS)

LONGITUDE CONVENTION : 1-360 WITH WEST 1-180 AND EAST 181-360

DO 101 I=1,NOPTS
LAMBDA(I)=AMOD((360.-LAMBDA(I)),360.)
IF (LAMBDA(I).EQ.0.) LAMBDA(I)=360.
CONTINUE

101

XW=AMOD((360.-XW1),360.)
XE=AMOD((360.-XE1),360.)

```

```

C
C
C
DO 12 I=1,NOPTS
LAMBDA(I)=LAMBDA(I)*DTR
PHI(I)=PHI(I)*DTR
12 CONTINUE
C
C
RMSP = 1.E70
SIGN = -1.
YICOUNT = 0.0
XJCOUNT = 0.0
COTALFP = 0.0
ALEPH = 0.0
MUOP = 0.0
NUOP = 0.0
MUAV = 0.0
AVER = 0.0
PHIC = 0.0
CPHI = 0.0
LAMBDA0 = 0.0
CLAMBDA = 0.0
C
PHI0 = PHI(1)
LAMBDA0 = LAMBDA(1)
C
DRY = (YN - YS)/6.
DRX = (XE - XW)/6.
XC = XW + (DRX * 3.)
YC = YS + (DRY * 3.)
IHEM = 1 ;SET FLAG TO NORTHERN HEMISPHERE
IF ((PHI0.LT.0.).AND.(PHI(NOPTS).LT.0.)) IHEM = 0 ;SOUTHERN HEMISPHERE
IF (IHEM.EQ.0) SIGN = 1.
C
C
DO 61 IJ = 1,9
C
C*****
C
DO 1661 I = 1,5
XI = FLOAT(I)
PHIC = YC - (2.*DRY) + ((XI - 1.) * DRY)
PHIC = PHIC * DTR
C
C*****
C
DO 1661 J = 1,5
XJ = FLOAT(J)
LAMBDA0 = XC - (2.*DRX) + ((XJ - 1.) * DRX)
LAMBDA0 = LAMBDA0 * DTR
CALL GTLOC (NU0, MU0, PHIC, LAMBDA0, PHI0, LAMBDA0)
AMU0 = ALOG(TAN(MU0*0.5))
SUM1 = 0.
SUM2 = 0.
SUM3 = 0.
SUM4 = 0.
NUP = NU0
C
C
DO 59 K = 1, NOPTS
CALL GTLOC( NUO(K), MUO(K), PHIC, LAMBDA0, PHI(K), LAMBDA(K))
IF (MUO(K).GT.MU0.AND.K.GT.(NOPTS/4)) GO TO 1661
IF (ABS(NUP-NUO(K)).GT.PI) NUO(K) = NUO(K)-(SIGN*2.*PI)

```

```

AMU(K) = ALOG(TAN(MUO(K)*0.5))-AMU0
SUM1 = SUM1 + NUO(K)
SUM2 = SUM2 + (NUO(K) * AMU(K))
SUM3 = SUM3 + AMU(K)
SUM4 = SUM4 + (AMU(K)*AMU(K))
NUP = NUO(K)
59 CONTINUE
C
C
CR=(XNOPTS*SUM4)-(SUM3*SUM3) ;DENOMINATOR
IF (CR .EQ. 0.) COTALF = 1.E70
IF (CR .EQ. 0.) NU0 = 1.E70
IF (CR .EQ. 0.) GO TO 567
COTALF=((SUM1*SUM3)-(XNOPTS*SUM2))/CR
NU0=((SUM1*SUM4)-(SUM2*SUM3))/CR
567 CONTINUE
C
RMS = 0.
MUSUM = 0.
C
C
DO 58 K = 1,NOPTS
MUSUM = MUSUM + MUO(K)
NUE = NU0 - (AMU(K) * COTALF)
RMS = ((NUE - NUO(K)) * (NUE - NUO(K))) + RMS
58 CONTINUE
C
RMS = SQRT(RMS/XNOPTS)
C
C****
C
IF (RMS .GE. RMSP) GO TO 1661
AVER = RMS/SQRT(XNOPTS)
MUAV = MUSUM/XNOPTS
RMSP = RMS
COTALFP = ABS(COTALF)
MU0P = MU0
NU0P = NU0
YICOUNT = FLOAT(I)
XJCOUNT = FLOAT(J)
CPHI = PHIC
CLAMBDA = LAMBDAC
C
1661 CONTINUE
C
YC = YC - (2.*DRY) + ((YICOUNT - 1.) * DRY)
XC = XC - (2.*DRX) + ((XJCOUNT - 1.) * DRX)
DRY = DRY*0.25
DRX = DRX*0.25
C
61 CONTINUE
C
CPHI = CPHI/DTR
CLAMBDA = -CLAMBDA/DTR
IF (CLAMBDA.LT.-180.) CLAMBDA=CLAMBDA + 360.
C
ALEPH = ATAN(1./COTALFP)
RADER = (MUAV*AVER)/(COTALFP*DTR)
C
C
C
C

```



```

TYPE
TYPE "RMS LOOP COMPLETE: GOOD LUCK! "
TYPE
TYPE
TYPE
TYPE
TYPE "PHIC.....",CPHI
TYPE "LMBDAC...",CLAMBDA
TYPE
TYPE "DRX.....", (DRX*4.)
TYPE "DRY.....", (DRY*4.)
TYPE
TYPE "COTALF...",COTALFP
TYPE "ALFA.....", (ALEPH/DTR)
TYPE
TYPE "NUØ.....", (NUØP/DTR)
TYPE "MUØ.....", (MUØP/DTR)
TYPE
TYPE "RMS.....",RMSP
TYPE "AVER.....", (AVER/DTR)
TYPE
TYPE "RADER....",RADER
TYPE "IN NM....", (RADER*6Ø.)

C
WRITE (18,1ØØØ)
WRITE (18,2ØØØ) CPHI,CLAMBDA
WRITE (18,3ØØØ) ALEPH/DTR,COTALFP
WRITE (18,5ØØØ) NUØP/DTR,MUØP/DTR
WRITE (18,6ØØØ) RMSP,AVER/DTR
WRITE (18,7ØØØ) RADER,RADER*6Ø.

C
C
C
C *****
C
TPC = 2. * PI * (COS(ALEPH) * COS(ALEPH))
NUMIN = NUØP + (SIGN * Ø.Ø5 * TPC)
RANGE = -SIGN * (TPC + (4. *PI))
PHIC = CPHI*DTR
LMBDAC = AMOD((36Ø.-CLAMBDA),36Ø.)*DTR
NPRS=1ØØ
XNPRS = FLOAT(NPRS)

C
C
C
C
CALCULATE THE FITTED SPIRAL
DO 667 K = 1,NPRS
XK = FLOAT(K)
NUEX = ((XK/XNPRS) * RANGE) + NUMIN
MUEX = 2.*ATAN(TAN(MUØP*Ø.5)*EXP((SIGN/COTALFP)*(NUEX-NUØP)))
CALL LTGEO (NUEX, MUEX, PHIC, LMBDAC, PHIX(K),LMBDAX(K))
PHIX(K) = PHIX(K)/DTR
LMBDAX(K) = -LMBDAX(K)/DTR
IF (LMBDAX(K).LT.-18Ø.) LMBDAX(K)=LMBDAX(K) + 36Ø.
667 CONTINUE

C
C
C
C
DRAW THE FITTED SPIRAL AFTER CONVERTING TO SCREEN COORDINATES
ICOLOR = 254 ;GREEN
CALL DWSPIR (PHIX,LMBDAX,IB,IBUF,NPRS,ICOLOR)

```



SUBROUTINE STAN  
OVERLAY OSTAN

C  
C

```
COMMON/PR/ DATE,FRMTIME,IHI,ILO,IRES
COMMON/HA/ UN(100),NOPTS
COMMON/SV/ IFLAG,IHEM,PHIS(20),XLAMS(20),COTALS(20)
COMMON/SCAT/ ICAT(256),PHI(100),XLAMBDA(100),IPIX(100),IRAS(100),
& FILL(57),AMP,M90,MAXH,V3
COMMON/F/ AMPM,AMP8,TVAR5,HEMVM,V32,TVAR8,V3M,X90M,THLDB,SD2
COMMON/HARM/ COTALF,XMU0,XNU0,PHIC,XLAMBDA
COMMON/BUFR1/ IER,IERR,ILINE(256),IOPT,NTYPE
COMMON/BUFR2/ JOB,IC(256),IB(256),NAME1(10)
COMMON/GF/ IBUF(256)
```

C  
C

```
REAL NU0,MU0,LAMBDA(100)
REAL NU,MU
REAL SD(20),BAR(20)
INTEGER MAX(20)
```

C

```
EQUIVALENCE (NU0,XNU0),(MU0,XMU0),(XLAMBDA(1),LAMBDA(1))
```

C

C

C

```
PI = 3.1415926535898
DTR = 0.0174533
```

C

C

```
NOPTS = 20 ;NUMBER OF HARMONICS
NSECT = 20 ;NUMBER OF ORTHOGONAL SLICES
```

C

```
DO 40 I=1,20
MAX(I) = 0
SD(I) = 0.0
BAR(I) = 0.0
CONTINUE
```

40

C

C

C

```
X90M = V3M = HEMVM = AMPM = 0.0
XLABDAC = -XLABDAC
IF (XLABDAC.LT.-PI) XLABDAC = (2.*PI) + XLABDAC
NOPTS = NOPTS*2
ICOLOR = 256 ;RED
```

C

C

```
DO 1 I=1,100
UN(I) = 0.0
CONTINUE
```

1

C

C

```
CALL CLOSE (1,IER)
CALL OPEN (1,NAME1,2.512,IER)
IF (IER.EQ.1) GO TO 5
TYPE"CANNOT OPEN IMAGE FILE, IER = ",IER
IER = 1
GO TO 999
```

C

C

5

```
ALEPH = ATAN(1./COTALF)
TPS = 2.*PI*(SIN(ALEPH)*SIN(ALEPH))
TPC = 2.*PI*(COS(ALEPH)*COS(ALEPH))
AMU0 = TAN(MU0*0.5)
```





```

C
C
DO 30 J=1,NOPTS
CALL RDBLK(1,IRAS(J),ICAT,1,IER)
IF (IER.EQ.1) GO TO 35
TYPE"CANNOT READ IMAGE FILE, IER = ",IER
IER = 1
GO TO 999

C
35 I HOLD = ICAT((IPIX(J)/2)+1)
IF (MOD(IPIX(J),2).EQ.0) I HOLD = ISHFT(I HOLD,-8)
IF (MOD(IPIX(J),2).NE.0) I HOLD = I HOLD.AND.377K
UN(J) = FLOAT(I HOLD)
UNBAR = UN(J) + UNBAR
CALL APOINT (IPIX(J),IRAS(J),ICOLOR)
30 CONTINUE

C
C
UNBAR = UNBAR/XNOPTS

C
DO 90 J=1,NOPTS
XSD = ((UNBAR-UN(J))*(UNBAR-UN(J))) + XSD
90 CONTINUE

C
C
S MAX = UNBAR - (1.5*SQRT(XSD/XNOPTS))
S MAX = AINT(S MAX)
UNBAR = 0.0
XSD = 0.0

C
C
DO 100 J=1,NOPTS
IF (UN(J).LT.S MAX) UN(J) = S MAX
UNBAR = UN(J) + UNBAR
100 CONTINUE

C
C
UNBAR = UNBAR/XNOPTS

C
DO 110 J=1,NOPTS
XSD = ((UNBAR-UN(J))*(UNBAR-UN(J))) + XSD
110 CONTINUE

C
SD(I) = SQRT(XSD/XNOPTS)
BAR(I) = UNBAR

C
C
MAX(I) = IFIX(S MAX)
IR MAXT = IFIX(S MAX)
IF (IR MAXT.GT.178) MAXT = 420 - IR MAXT
IF (IR MAXT.LE.178) MAXT = (662 - IR MAXT)/2
MAXT = MAXT - 273

C
C
CALL WLT (IBUF,256,0)
CALL XMT (0)
CALL HARMON

C
C
X90M = FLOAT(M90)+X90M
V3M = V3+V3M
HEMVM = FLOAT(MAXH)+HEMVM

```

```

      AMPM = AMP+AMPM
      IF (I.EQ.16) AMP8 = AMP
      IF (I.EQ.4) V32 = V3
C
10  CONTINUE
C
      TVAR5 = SD(10)*SD(10)
      TVAR8 = SD(16)*SD(16)
      THLD8 = MAX(16)
      SD2 = SD(4)
      X90M = X90M/20.
      V3M = V3M/20.
      HEMVM = HEMVM/20.
      AMPM = AMPM/20.

      WRITE TO THE PARAMETER FILE:

      BAR(I) = AVERAGE VALUE OF SLICE
      MAX(I) = MINIMUM IRCOUNT USED IN ANALYSIS
      SD(I) = STANDARD DEVIATION OF SLICE

      WRITE (21,7000) (BAR(I),I=1,20)
      WRITE (21,6000) (MAX(I),SD(I),I=1,20)

X3000  FORMAT(F6.0,I2,2I3,F6.2,F7.2,F6.2,2F5.2)
X4000  FORMAT("DECK",1X,10A2)
X6000  FORMAT(10(I3,F5.2))
X7000  FORMAT (10F8.3,/,10F8.3)
C
      CALL FCST
C
999  CALL CLOSE (1,IERR)
      CALL OVEXIT ("OSTAN",IERR)
      IF (IERR.NE.1) TYPE"OSTAN EXIT ERROR : ",IERR
      END

```

F8.3  
I3  
F5.2

APPENDIX B  
GOVERNING EQUATIONS

The slope of a line on the surface of a sphere is given by

$$\text{SLOPE} = A = \frac{\partial \phi}{\partial \theta} \sin \theta \quad (\text{B1})$$

or

$$A = \frac{\partial \phi}{\partial \ln \tan(\frac{\theta}{2})}, \quad (\text{B2})$$

where  $\phi$  is longitude and  $\theta$  is colatitude. By definition  $A$  is constant for a spherical-log spiral. Figure B1 shows the relationship between the longitudinal coordinate  $\phi$  and  $\theta$ , the colatitude.

Separating the variables in (B2) and integrating from the outermost point  $(\phi_0, \theta_0)$  of a spiral in towards the center, we get the equation for a line of constant slope on a sphere

$$\int_{\phi_0}^{\phi} d\phi = A \int_{\ln \tan(\frac{\theta_0}{2})}^{\ln \tan(\frac{\theta}{2})} d \ln \tan(\frac{\theta}{2})$$

and we obtain

$$\phi - \phi_0 = A [\ln \tan(\frac{\theta}{2}) - \ln \tan(\frac{\theta_0}{2})]$$

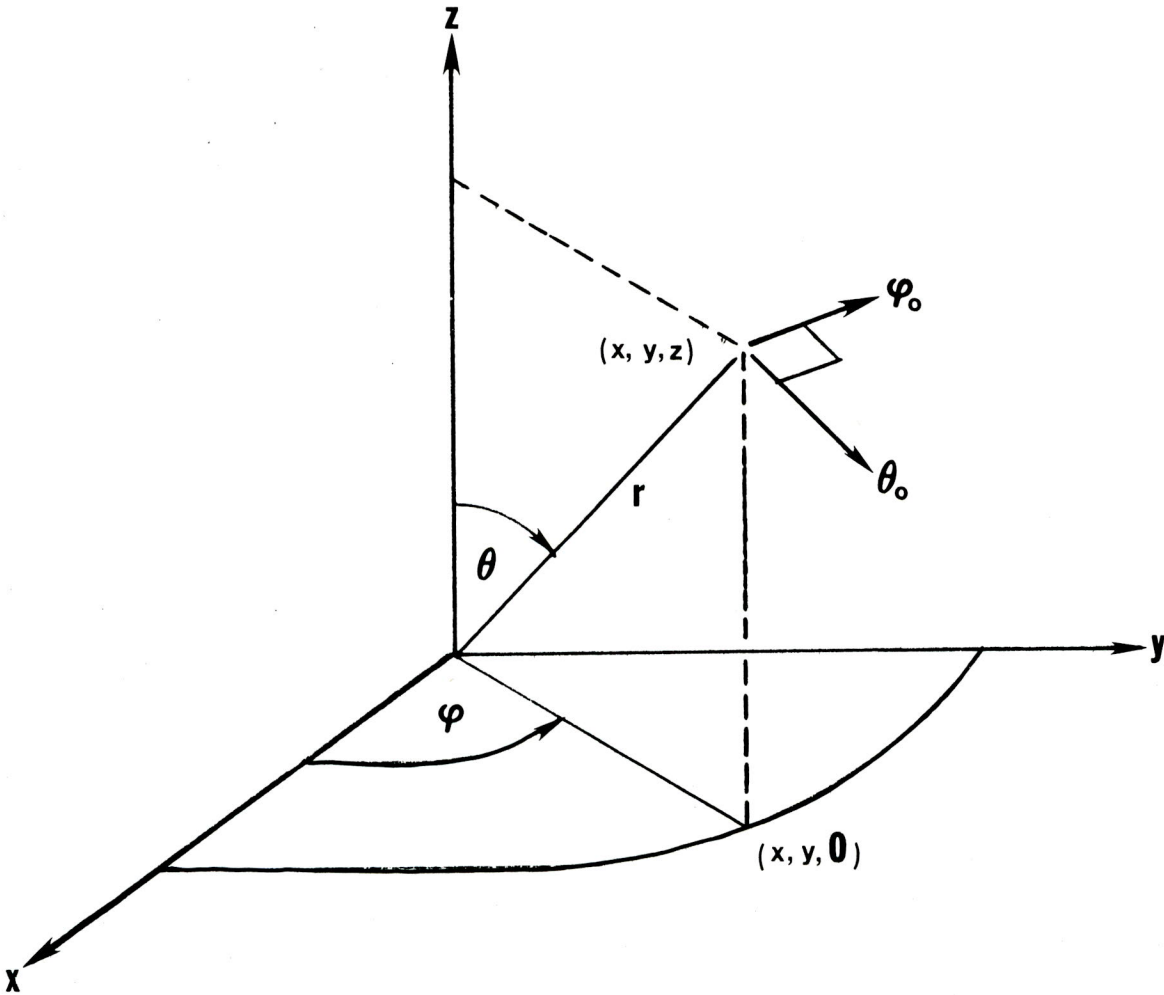


Figure B1. Spherical polar coordinates showing the relationship between  $\phi$  and  $\theta$ .  $r$  is constant on the surface of a sphere.  $\phi_o$  and  $\theta_o$  are the unit vectors.



or

$$\phi - \phi_0 = A \ln \left[ \frac{\tan(\frac{\theta}{2})}{\tan(\frac{\theta_0}{2})} \right]. \quad (B3)$$

Renaming the variables:

$v \equiv \phi$  the azimuthal coordinate

and  $\mu \equiv \theta$  the radial coordinate

and defining the constant,  $A \equiv -\cot \alpha$ , where  $\alpha$  is the spiral inflow angle, (B3) becomes

$$v - v_0 = -\cot \alpha \ln \left[ \frac{\tan(\frac{\mu}{2})}{\tan(\frac{\mu_0}{2})} \right]$$

or

$$v = v_0 - \cot \alpha \ln \left[ \frac{\tan(\frac{\mu}{2})}{\tan(\frac{\mu_0}{2})} \right] \quad (B4)$$

and

$$\mu = 2 \arctan \left\{ \tan(\frac{\mu_0}{2}) \exp[-\tan \alpha (v - v_0)] \right\} \quad (B5)$$

Equation (B5) is the equation for a logarithmic spiral decreasing with increasing azimuth and having a constant inflow angle ( $\alpha$ ) on the surface of a sphere. Equation (B4)

is in the form of an equation for a line:

$$y = mx + b \quad (B6)$$

where:

$$y = v,$$

$$x = \ln \left[ \frac{\tan(\frac{\mu}{2})}{\tan(\frac{\mu_0}{2})} \right],$$

$$b = v_0, \text{ and}$$

$$m = -\cot \alpha.$$

Therefore, all points along a spiral,  $\mu_i$  and  $v_i$ , can be plotted on a cartesian graph with abscissa  $\ln[(\tan(\mu/2))/(\tan(\mu_0/2))]$  and ordinate  $v$ ; and a spherical-log spiral would be represented by a straight line with slope  $-\cot \alpha$ . To map any point on the surface of a sphere into the spiral coordinates the latitude-longitude representation of the point must be converted to  $\mu$  and  $v$ , the great circle distance between the point and the spiral center and their angular separation, respectively.

In order to specify the spiral coordinates the spiral center is needed and is furnished by convergent search routine which returns a best fit center in a least squares sense. The problem of fitting the best least squares line to a collection of data involves minimizing

$$\sum_{i=1}^N [Y_i - (mX_i + b)]^2$$

with respect to  $m$  and  $b$ .

Equation (B6) yields the normal equations, which must be satisfied for a minimum to occur.

$$\left. \begin{aligned} m \sum_{i=1}^N X_i^2 + b \sum_{i=1}^N X_i &= \sum_{i=1}^N X_i Y_i \\ \text{and} \\ m \sum_{i=1}^N X_i + bN &= \sum_{i=1}^N Y_i \end{aligned} \right\} \quad (B7)$$

where:

$$m = - \cot \alpha$$

$$X_i = \ln \left[ \frac{\tan(\frac{\mu_i}{2})}{\tan(\frac{\mu_0}{2})} \right]$$

$$b = v_0$$

$$Y_i = v_i$$

The solution to (B7) is the following:

$$\begin{aligned}
 m &= \frac{N \sum_{i=1}^N X_i Y_i - \sum_{i=1}^N X_i \sum_{i=1}^N Y_i}{N \sum_{i=1}^N X_i^2 - \left( \sum_{i=1}^N X_i \right)^2} \\
 \text{and} \quad b &= \frac{\sum_{i=1}^N X_i^2 \sum_{i=1}^N Y_i - \sum_{i=1}^N X_i Y_i \sum_{i=1}^N X_i}{N \sum_{i=1}^N X_i^2 - \left( \sum_{i=1}^N X_i \right)^2}
 \end{aligned} \quad \left. \vphantom{\begin{aligned} m \\ b \end{aligned}} \right\} \quad (B8)$$

From the estimated center and  $\mu_0$ ,  $v_0$  and  $\alpha$  are calculated using the above linear least squares fit. Using the resulting spiral parameters the RMS error is calculated for the input points and used as the criterion for converging on a more accurate guess of the spiral center.

The convergent search routine divides the area estimated to contain the spiral center into a six-by-six grid. Each of the twenty-five interior grid points are used as sample spiral centers and the RMS error calculated. The grid point with the smallest RMS error is then focused on as the new grid center and the grid size divided by six. The process is iterated nine times, with the final center the best fit (smallest RMS error).

The equation for an orthogonal spiral is just (B6) with  $m$  replaced by  $-\frac{1}{m}$ ,



$$y = -\frac{1}{m} x + b$$

or, in spiral notation

$$v = \frac{\ln \left[ \frac{\tan(\frac{\mu}{2})}{\tan(\frac{\mu_0}{2})} \right]}{\cot \alpha} + v_0 . \quad (B9)$$

## APPENDIX C

### DESCRIPTION OF CYCLONES OF DEPENDENT DATA SET

#### 1. DOLORES

Hurricane Dolores was the sixth tropical cyclone of the Eastern North Pacific (ENP) 1979 season. The initial disturbance was spawned west of the Central American coast on 14 July over 29°C water. The disturbance was upgraded to a tropical depression by 0600 GMT 17 July and further to a tropical storm by 1800 GMT 17 July as the winds increased above 35 kt. By the next day the winds had increased to above 65 kt and Hurricane Dolores was born. At this time it changed course from westerly to north-westerly, and began a rapid intensification. An eye became visible on satellite photographs by 1800 GMT 19 July and by 0000 GMT 21 July Dolores had reached her maximum intensity with winds of over 105 kt. Accelerating around an upper level high-pressure area centered over Mexico, Dolores moved to a position thirteen degrees west of the Baja California coast and began to weaken over cool water. By 1800 GMT 22 July, Dolores was downgraded to a tropical depression and finally dissipated with a cloud mass lingering in the Pacific for three days.

#### 2. ENRIQUE

Hurricane Enrique, the seventh tropical cyclone of the ENP 1979 season, developed as a tropical disturbance near

10° N, 108° W on 17 August. At 1800 GMT that day the disturbance was upgraded to a tropical depression and by 0000 GMT 18 August was upgraded again to Tropical Storm Enrique. At 0000 GMT 19 August the west-northwestward moving Enrique was declared Hurricane Enrique and began to show an eye on satellite photographs. The maximum winds, 70 kt, decreased to 55 kt by 0600 GMT 21 August as then Tropical Storm Enrique moved over low clouds and cool water. However, by 1700 GMT that same day the storm was upgraded to hurricane status again as the winds increased above 70 kt. Enrique's development was now rapid as it reached its maximum intensity at 1200 GMT 22 August with winds of 125 kt. Enrique began to weaken as it moved over cool water and low clouds, and by 1200 GMT 23 August was downgraded back to tropical storm status. By 0000 GMT 24 August the storm was further downgraded to a tropical depression and weakened rapidly, dissipating over the next two days.

### 3. DAVID

David was the fourth hurricane in the Atlantic 1979 season. It organized in the mid-tropical Atlantic and was declared a tropical depression by 0000 GMT 25 August. Tracking westward around the southern portion of the Bermuda High, the disturbance was upgraded to a tropical storm by 1800 GMT 25 August. The storm continued its steady increase in intensity and was upgraded to hurricane strength

by 1800 GMT 26 August. Hurricane David continued its development and west-northwestward movement and reached the eastern coast of Hispaniola on 31 August with a central pressure of approximately 925 mb and estimated winds in excess of 150 kt. Flooding caused by the excessive rainfall from David was responsible for over 2000 deaths and over 1 billion dollars damage on Hispaniola (Hebert, 1980). David continued its clockwise track and entered Florida by early 3 September with winds in excess of 80 kt. David weakened slowly over land, causing 15 deaths, damages of 320 million dollars and evacuations of 400,000 people (Hebert, 1980). David was finally downgraded to tropical storm status over South Carolina at 1800 GMT 4 September. Tropical storm David was further downgraded to depression stage on 6 September as its winds fell below 35 kt and central pressure increased to 992 mb. Strong winds from the remains of Hurricane David continued to persist along the Atlantic seaboard all the way into the Canadian provinces.

#### 4. FREDERIC

Hurricane Frederic started life as an African tropical wave on 27 August and turned out to be the sixth hurricane of the 1979 Atlantic season. The wave continued to develop and reached tropical depression stage by 1800 GMT 28 August; the disturbance became Tropical Storm Frederic by 0000 GMT 30 August while continuing on its western track. At 1800



GMT 31 August Tropical Storm Frederic became Hurricane Frederic in the same area of the Atlantic that David had done four days before; an eye became visible on the satellite imagery. However, Frederic began to interact with the, by then, immense outflow from David and weakened back to tropical storm status. Frederic passed over Puerto Rico and further weakened to depression stage by 0600 GMT 6 September. The disturbance then turned northwestward around the high and strengthened back to tropical storm intensity by 0000 GMT 9 September off of the southern coast of Cuba. Freed from the influence of David, Frederic regained hurricane force over western Cuba with a central pressure 990 mb at 1200 GMT 10 September. Hurricane Frederic continued to develop and passed over the Gulf Coast of the United States with a central pressure of 946 mb, and winds of approximately 115 kt, at 0300 GMT 13 September. Frederic caused over 2.3 billion dollars damage in the United States, making it the costliest hurricane in history for the United States (Hebert, 1980). Hurricane Frederic quickly filled and was degraded to tropical storm status over Mississippi by 1200 GMT 13 September. Frederic's remnants continued to track over the Midwest, dissipating to depression status by 1200 GMT 14 September and exiting into Canada by 0000 GMT 15 September.

## 5. GLORIA

Gloria was the seventh hurricane of the Atlantic 1979 season and was the first of the season not to affect a landfall. The disturbance started as a well organized African tropical wave and was classified as a tropical depression at 1200 GMT 4 September. The depression moved into the mid-Atlantic and became Tropical Storm Gloria by 1200 GMT 6 September. By 0000 GMT 7 September Gloria was upgraded to hurricane strength and started to move northwestward in the mid-Atlantic. Gloria intensified for a day, weakened briefly, then regained intensity until it reached its lowest central pressure of 975 mb on 1800 GMT 12 September. Gloria then began to fill and move northeastward and was downgraded to a tropical storm by 0600 GMT 15 September and eventually merged with an extratropical low pressure system northwest of the Azores by late that day.

## 6. IGNACIO

Hurricane Ignacio was the twelfth, of thirteen, tropical cyclone of the ENP 1979 season. It began as a tropical disturbance off of the Central American coast, reached tropical depression status by 1800 GMT 23 October positioned near 12° N, 95° W. The depression increased in intensity while over warm water and was declared Tropical Storm Ignacio at 1200 GMT 24 October. The storm moved west for

a day, then northwest, paralleling the Mexican coast, and was upgraded to Hurricane Ignacio by 1800 GMT 26 October as its winds increased to 70 kt. Ignacio reached its maximum intensity by 2200 GMT 27 October near 17° N, 106° W.

Ignacio continued to move northwest for a day then recurved and began to weaken. The hurricane was downgraded to tropical storm status by 1800 GMT 29 October as the winds dwindled past 55 kt. By 1200 GMT 30 October the storm was downgraded to a tropical depression and brought a landfall over the Central Mexican coast slightly north of Acapulco.

## REFERENCES

- Afifi, A.A. and S.P. Azen, 1979: Statistical Analysis, Academic Press, N.Y., 442 pp.
- Akima, H., 1970: A New Method of Interpolation and Smooth Curve Fitting Based on Local Procedures. J. Assoc. Comput. Mach., 17, 589-602.
- Anthes, R.A., 1982: Tropical Cyclones--Their Evolution, Structure and Effects. Amer. Meteor. Soc., 208 pp.
- Arnold, C.P., 1977: Tropical Cyclone Cloud and Intensity Relationships. Colo. State Univ., Atmos. Sci. Paper No. 277, Ft. Collins, CO, 154 pp.
- Black, P.G. and R.A. Anthes, 1971: On the Asymmetric Structure of the Tropical Cyclone Outflow Layer. J. Atmos. Sci., 28, 1348-1366.
- Blackman, R.B. and J.W. Tukey, 1958: The Measurement of Power Spectra. Dover Pub., N.Y., 190 pp.
- Brown, M.B. and A.B. Forsythe, 1974: Robust Tests for the Equality of Variances. Journal of the American Statistical Association, 69, 364-367.
- Browner, S.P., W.L. Woodley, and C.G. Griffith, 1977: Diurnal Oscillation of the Area of Cloudiness Associated with Tropical Storms. Mon. Wea. Rev., 105, 856-864.
- Dixon, W.J., 1981: BMDP Statistical Software 1981. Univ. Cal. Press, Berkeley, 725 pp.
- Dvorak, V.F., 1973: A Technique for the Analysis and Forecasting of Tropical Cyclone Intensities From Satellite Pictures. NOAA Technical Memorandum NESS 45 (Revision of NOAA TM NESS 36). U.S. Dept. of Commerce, Suitland, MD, 19 pp.
- \_\_\_\_\_, 1975: Tropical Cyclone Intensity Analysis and Forecasting from Satellite Imagery. Mon. Wea. Rev., 103, 420-430.
- \_\_\_\_\_, 1979: Tropical Cyclone Intensity Analysis Using Either EIR or VIS Imagery. Training Notes, May 1979, 26 pp.



- Erickson, C.O., 1972: Evaluation of a Technique for the Analysis and Forecasting of Tropical Cyclone Intensities From Satellite Pictures. NOAA Technical Memorandum NESS 42. U.S. Dept. of Commerce, Suitland, MD, 28 pp.
- Fett, R.W., 1966: Upper-Level Structure of the Formative Tropical Cyclone. Mon. Wea. Rev., 94, 9-18.
- Fritz, S., L.F. Hubert, and A. Timchalk, 1966: Some Inferences from Satellite Pictures of Tropical Disturbances. Mon. Wea. Rev., 94, 231-236.
- Gentry, R.C., E. Rodgers, J. Steranka, and W.E. Shenk, 1980: Predicting Tropical Cyclone Intensity Using Satellite-Measured Equivalent Blackbody Temperature of Cloud Tops. Mon. Wea. Rev., 108, 445-455.
- Gunther, E.B., 1980: Eastern North Pacific Tropical Cyclones of 1979. Mon. Wea. Rev., 108, 631-641.
- Hebert, P.J., 1980: Atlantic Hurricane Season of 1979: Mon. Wea. Rev., 108, 973-990.
- Hubert, L.F., A. Timchalk and S. Fritz, 1969: Estimating Maximum Wind Speed of Tropical Storms from High Resolution Infrared Data. ESSA Tech. Rep. NES50, 33 pp.
- Kurihara, Y., 1976: On the Development of Spiral Bands in a Tropical Cyclone. J. Atmos. Sci., 33, 940-958.
- Lahiri, A., 1981: A Study of Cloud Spirals of Tropical Cyclones. Mausam, 32, 155-158.
- Nicholson, F.H., 1982: Typhoon IR Response Determination. Systems Control Technology, Inc., Project 6457, Rept. No. N62271-81-M-2095, 18 pp.
- Panofsky, H.A. and G.W. Brier, 1968: Some Applications of Statistics to Meteorology. Pennsylvania State University Press, 224 pp.
- Peterson, V.L., A.N. Hull and C.J. Lozano, 1983: A Search for a Tropical Cyclone Spiral Intensity Change Algorithm. Global Weather Dynamics, Inc., Rept. No. N00228-82-C-8107, 34 pp.
- Rodgers, E. and R.C. Gentry, 1983: Monitoring Tropical Cyclone Intensity Using Environmental Wind Fields Derived From Short-Interval Satellite Images. Mon. Wea. Rev., 11, 979-996.

- Schramm, W., P. Zeleny, R. Nagle, and A. Weinstein, 1982: The Navy SPADS, A Second Generation Environmental Display System. Ninth Conference on Weather Forecasting and Analysis, Seattle, WA, AMS, 72-75.
- Senn, H.V. and H.W. Hiser, 1959: On the Origin of Hurricane Spiral Rain Bands. J. Meteor., 16, 419-426.
- Sheets, R.C. and P.G. Grieman, 1975: An Evaluation of the Accuracy of Tropical Cyclone Intensities and Locations Determined from Satellite Pictures. NOAA Technical Memorandum ERL WMPO-20, U.S. Department of Commerce, Boulder, CO, 43 pp.
- Shewchuk, J.D. and R.C. Weir, 1980: An Evaluation of the Dvorak Technique for Estimating Tropical Cyclone Intensities from Satellite Imagery. U.S. Naval Oceanography Command Center Joint Typhoon Warning Center NOCC/JTWC 80-2. Naval Oceanography Command, NSTL Station, Bay St. Louis, MS, 25 pp.
- Swadley, S.D., 1983: Evaluation of the Tropical Cyclone Spiral Linearization Technique. NAVENVPREDRSCHFAC Tech. Rept. 83-04, 42 pp.
- Willoughby, H.E., 1978: A Possible Mechanism for the Formation of Hurricane Rain Bands. J. Atmos. Sci., 35, 838-848.

#### ACKNOWLEDGEMENTS

The author wishes to thank Dr. Ted Tsui, NAVENVPRED-RSCHFAC for his suggestion and support of this research project, and Dr. Peter Lester, San Jose State University for his continuous time and effort in reading the manuscript. The author also wishes to thank Dr. Francis Nicholson of Systems Control Technology, Inc., and Mr. Stephen Swadley, NAVENVPREDRSCHFAC for their many helpful suggestions for the computer program and for the interpretation of the results. The author also appreciates the editorial comments from Mr. Stephen Bishop, NAVENVPREDRSHFAC and graphic art service from DML Frank Hermoso, NAVENVPREDRSCHFAC.

DISTRIBUTION

COMMANDER IN CHIEF  
U.S. ATLANTIC FLEET  
ATTN: FLT METEOROLOGIST  
NORFOLK, VA 23511

COMMANDER IN CHIEF  
U.S. PACIFIC FLEET  
CODE 02M  
PEARL HARBOR, HI 96860

COMTHIRDFLT  
CODE N33  
PEARL HARBOR, HI 96860

COMSEVENTHFLT  
ATTN: FLT METEOROLOGIST, N30W  
FPO SAN FRANCISCO 96601

CHIEF OF NAVAL RESEARCH (2)  
LIBRARY SERVICES, CODE 734  
RM 633, BALLSTON TOWER #1  
800 QUINCY ST.  
ARLINGTON, VA 22217

OFFICE OF NAVAL RESEARCH  
CODE 422AT  
ARLINGTON, VA 22217

OFFICE OF NAVAL RESEARCH  
CODE 420  
ARLINGTON, VA 22217

OFFICE OF NAVAL RESEARCH  
COASTAL SCIENCES PROGRAM  
CODE 422 CS  
ARLINGTON, VA 22217

CHIEF OF NAVAL OPERATIONS  
(OP-952)  
U.S. NAVAL OBSERVATORY  
WASHINGTON, DC 20390

CHIEF OF NAVAL OPERATIONS  
NAVY DEPT. OP-986G  
WASHINGTON, DC 20350

NAVAL DEPUTY TO THE  
ADMINISTRATOR, NOAA  
ROOM 200, PAGE BLDG. #1  
3300 WHITEHAVEN ST. NW  
WASHINGTON, DC 20235

OFFICER IN CHARGE  
U.S. NAVOCEANCOMDET  
APO SAN FRANCISCO 96519

OFFICER IN CHARGE  
U.S. NAVOCEANCOMDET  
FLEET ACTIVITIES  
FPO SEATTLE 98770

COMMANDING OFFICER  
NAVAL RESEARCH LAB  
ATTN: LIBRARY, CODE 2620  
WASHINGTON, DC 20390

COMMANDING OFFICER  
NORDA  
NSTL STATION, MS 39529

COMMANDER  
NAVAL OCEANOGRAPHY COMMAND  
NSTL, MS 39529

COMMANDING OFFICER  
FLENUMOCEANCEN  
MONTEREY, CA 93940

COMMANDING OFFICER (2)  
NAVWESTOCEANCEN  
BOX 113  
PEARL HARBOR, HI 96860

COMMANDING OFFICER  
NAVEASTOCEANCEN  
MCADIE BLDG. (U-117)  
NAVAL AIR STATION  
NORFOLK, VA 23511

COMMANDING OFFICER  
NAVPOLAROCEANCEN  
NAVY DEPT.  
4301 SUITLAND RD.  
WASHINGTON, DC 20390

COMMANDING OFFICER  
U.S. NAVOCEANCOMCEN  
BOX 12, COMNAV Marianas  
FPO SAN FRANCISCO 96630

COMMANDING OFFICER  
U.S. NAVOCEANCOMFAC  
FPO SEATTLE 98762

COMMANDING OFFICER  
U.S. NAVOCEANCOMFAC  
BOX 63, NAS (CUBI PT)  
FPO SAN FRANCISCO 96654

SUPERINTENDENT  
LIBRARY REPORTS  
U.S. NAVAL ACADEMY  
ANNAPOLIS, MD 21402



NAVAL POSTGRADUATE SCHOOL  
METEOROLOGY DEPT.  
MONTEREY, CA 93943

LIBRARY  
NAVAL POSTGRADUATE SCHOOL  
MONTEREY, CA 93943

COMMANDER (2)  
NAVAIRSYSCOM  
ATTN: LIBRARY (AIR-7226)  
WASHINGTON, DC 20361

COMMANDER  
NAVAIRSYSCOM (AIR-330)  
WASHINGTON, DC 20361

COMMANDER  
NAVAIRSYSCOM  
MET. SYS. DIV. (AIR-553)  
WASHINGTON, DC 20360

COMMANDER  
AWS/DN  
SCOTT AFB, IL 62225

USAFETAC/TS  
SCOTT AFB, IL 62225

AFGL/LY  
HANSKOM AFB, MA 01731

DET 4 HQ AWS/CC  
APO SAN FRANCISCO 96334

DET 5 1WW/CC  
APO SAN FRANCISCO 96274

DIRECTOR (12)  
DEFENSE TECH. INFORMATION  
CENTER, CAMERON STATION  
ALEXANDRIA, VA 22314

ENVIRONMENTAL SERVICES DIV.  
OFFICE OF THE JOINT CHIEFS  
OF STAFF  
THE PENTAGON  
WASHINGTON, DC 20301

NOAA-NESDIS LIAISON  
ATTN: DR. M. HELFERT, CODE SC2  
NASA-JOHNSON SPACE CENTER  
HOUSTON, TX 77058

DIRECTOR  
NATIONAL EARTH SAT. SERV/SEL  
FB-4, S321B  
SUITLAND, MD 20233

DIRECTOR  
NATIONAL HURRICANE CENTER  
NOAA, GABLES ONE TOWER  
1320 S. DIXIE HWY  
CORAL GABLES, FL 33146

CHIEF, SCIENTIFIC SERVICES  
NWS/NOAA, SOUTHERN REGION  
ROOM 10E09  
819 TAYLOR ST.  
FT. WORTH, TX 76102

CHIEF, SCIENTIFIC SERVICES  
NWS/NOAA, WESTERN REGION  
P.O. BOX 11188,  
FEDERAL BLDG.  
SALT LAKE CITY, UT 84111

CHIEF, SCIENTIFIC SERVICES  
NWS, PACIFIC REGION  
P.O. BOX 50027  
HONOLULU, HI 96850

METEOROLOGIST IN CHARGE  
WEA. SERV. FCST. OFFICE, NOAA  
660 PRICE AVE.  
REDWOOD CITY, CA 94063

METEOROLOGIST IN CHARGE  
WEA. SERV. FCST. OFFICE, NOAA  
HONOLULU INTL. AIRPORT  
HONOLULU, HI 96819

DIRECTOR, CENTRAL PACIFIC  
HURRICANE CENTER NWS, NOAA  
HONOLULU, HI 96819

CHIEF  
MESOSCALE APPLICATIONS BRANCH  
NATIONAL EARTH SAT. SERV.  
1225 W. DAYTON  
MADISON, WI 53562

DIRECTOR (AOML)  
NATIONAL HURRICANE RSCH. LAB.  
1320 S. DIXIE HWY.  
CORAL GABLES, FL 33146

DIRECTOR  
TECHNIQUES DEVELOPMENT LAB  
GRAMAX BLDG.  
8060 13TH ST.  
SILVER SPRING, MD 20910

LABORATORY FOR ATMOS. SCI.  
NASA GODDARD SPACE FLIGHT CEN.  
GREENBELT, MD 20771

COLORADO STATE UNIVERSITY  
ATMOSPHERIC SCIENCES DEPT.  
ATTN: DR. WILLIAM GRAY  
FORT COLLINS, CO 80523

CHAIRMAN, METEOROLOGY DEPT.  
CALIFORNIA STATE UNIVERSITY  
SAN JOSE, CA 95192

COLORADO STATE UNIVERSITY  
ATMOSPHERIC SCIENCES DEPT.  
ATTN: LIBRARIAN  
FT. COLLINS, CO 80523

CHAIRMAN, METEOROLOGY DEPT.  
METEORO. & SPACE SCI. BLDG.  
1225 W. DAYTON ST.  
MADISON, WI 53706

DIRECTOR, REMOTE SENSING LAB  
UNIVERSITY OF MIAMI  
P.O. BOX 248003  
CORAL GABLES, FL 33124

CHAIRMAN, METEOROLOGY DEPT.  
PENNSYLVANIA STATE UNIV.  
503 DEIKE BLDG.  
UNIVERSITY PARK, PA 16802

FLORIDA STATE UNIVERSITY  
ENVIRONMENTAL SCIENCES DEPT.  
TALLAHASSEE, FL 32306

UNIVERSITY OF HAWAII  
METEOROLOGY DEPT.  
2525 CORREA ROAD  
HONOLULU, HI 96822

UNIVERSITY OF MARYLAND  
METEOROLOGY DEPT.  
COLLEGE PARK, MD 20742

R. CECIL GENTRY  
DEPT. OF PHYSICS & ASTRONOMY  
CLEMSON UNIVERSITY  
CLEMSON, SC 29631

THE EXECUTIVE DIRECTOR  
AMERICAN METEORO. SOCIETY  
45 BEACON ST.  
BOSTON, MA 02108

AMERICAN METEORO. SOCIETY  
METEOR. & GEOASTRO. ABSTRACTS  
P.O. BOX 1736  
WASHINGTON, DC 20013

MR. W. G. SCHRAMM/WWW  
WORLD METEOROLOGICAL  
ORGANIZATION  
CASE POSTALE #5, CH-1211  
GENEVA, SWITZERLAND

DIRECTOR, JTWC (3)  
BOX 17  
FPO SAN FRANCISCO 96630

BUREAU OF METEOROLOGY  
BOX 1289K, GPO  
MELBOURNE, VIC, 3001  
AUSTRALIA

METEOROLOGICAL INSTITUTE  
KYOTO UNIVERSITY  
ATTN: DR. R. YAMAMOTO  
SAKYO, KYOTO 606, JAPAN

LIBRARIAN, NEW ZEALAND  
METEOROLOGICAL SERVICE  
P.O. BOX 722  
WELLINGTON, NEW ZEALAND

DIRECTOR, TYPHOON MODERATION  
RSCH & DEV. OFFICE, PAGASA  
MINISTRY OF NATIONAL DEFENSE  
1424 QUEZON AVE.  
QUEZON CITY, PHILIPPINES